

Table of Contents

1. Supplemental figures and experimental methods.....	2
1.1. Characterization of TiO ₂ nanorods.....	2
1.2. Physical picture of the dual oxidation-reduction activity of high efficiency sites on bare TiO ₂ nanorods for photoelectrochemical water oxidation.....	3
1.3. Estimation of the deposited Co-B _i OEC amount by analyzing SEM images.....	4
1.4. Electrochemical flow cell design.....	5
1.5. Diffraction-limited sub-nanorod photocurrent measurements.....	5
2. Detailed data analysis procedures after single-molecule super-resolution localization analysis of fluorescence images.....	7
2.1. Single-molecule fluorescence image analysis for super-resolution localization.....	7
2.2. Filtering candidate molecules by their PSF width and quantitative single-molecule counting algorithm.....	9
2.3. Correcting for single product molecules adsorbed on the surface for more than one frame.....	11
2.4. Mapping the nanorod structural contour from SEM onto the super resolution single-molecule reaction images.....	12
3. Analysis of <i>i</i>-<i>E</i> data with the Gärtner-Butler model.....	14
3.1. Introduction to the Gärtner Model.....	14
3.2. Gärtner model for an <i>n</i> -type photoelectrode with minimal light absorption within <i>W</i> and negligible photocurrent contribution from carriers generated for <i>x</i> > <i>W</i>	15
3.3. Light absorption of an individual rutile TiO ₂ nanorod under focused laser excitation.....	16
The nano-optical effect of the nanorod is considered later in Section 5.8.....	17
3.4. η is the absorbed photon to current efficiency within the depletion layer and it also characterizes the local photocurrent efficiency at a nanorod spot.....	17
3.5. Flat band potential is traditionally measured under dark conditions ²⁴ , while our measurements are performed under illumination, so we replace E_{fb} with $E_{on,GB}$, the photocurrent onset potential predicted by the Gärtner-Butler model.....	17
3.6. Estimating N_d for these TiO ₂ nanorods.....	17
4. Analysis of single-molecule rate data versus applied potential.....	18
4.1. Kinetic model for the photoelectrocatalytic oxidation of AR.....	18
4.2. Kinetic model for the photoelectrocatalytic reduction of Rz.....	23
4.3. Procedures for fitting the potential dependences of AR oxidation and Rz reduction rates.....	25
4.4. Determining an ensemble-averaged v_c from ensemble i_{cath} - <i>E</i> data.....	26
5. Additional Supplementary Data and Discussions.....	26
5.1. Quantitative super-resolution reaction imaging reveals reaction rate patterns and spatially correlated h^+ and e^- reactions.....	26
5.2. There is no significant difference between $E_{on,GB}$ determined from <i>i</i> - <i>E</i> data and that from v_{AR} and v_{Rz} versus <i>E</i> data.....	28
5.3. The low average η value could be attributed to poor charge transport and inefficient charge transfer kinetics.....	29
5.4. $E_{on,GB}$ is linearly correlated with $E_{on,ss}$, and thus values and changes of $E_{on,GB}$ reflect directly the values and changes of $E_{on,ss}$	30
5.5. Co-B _i OEC deposition effects: 1) larger increase in η for nanorod spots with smaller initial η , and 2) larger negative shifts in $E_{on,GB}$ for nanorod spots with initially more positive $E_{on,GB}$	31
5.6. The large heterogeneity in η is likely <i>not</i> due to heterogeneity of contact resistances between individual nanorods and the ITO electrode.....	31

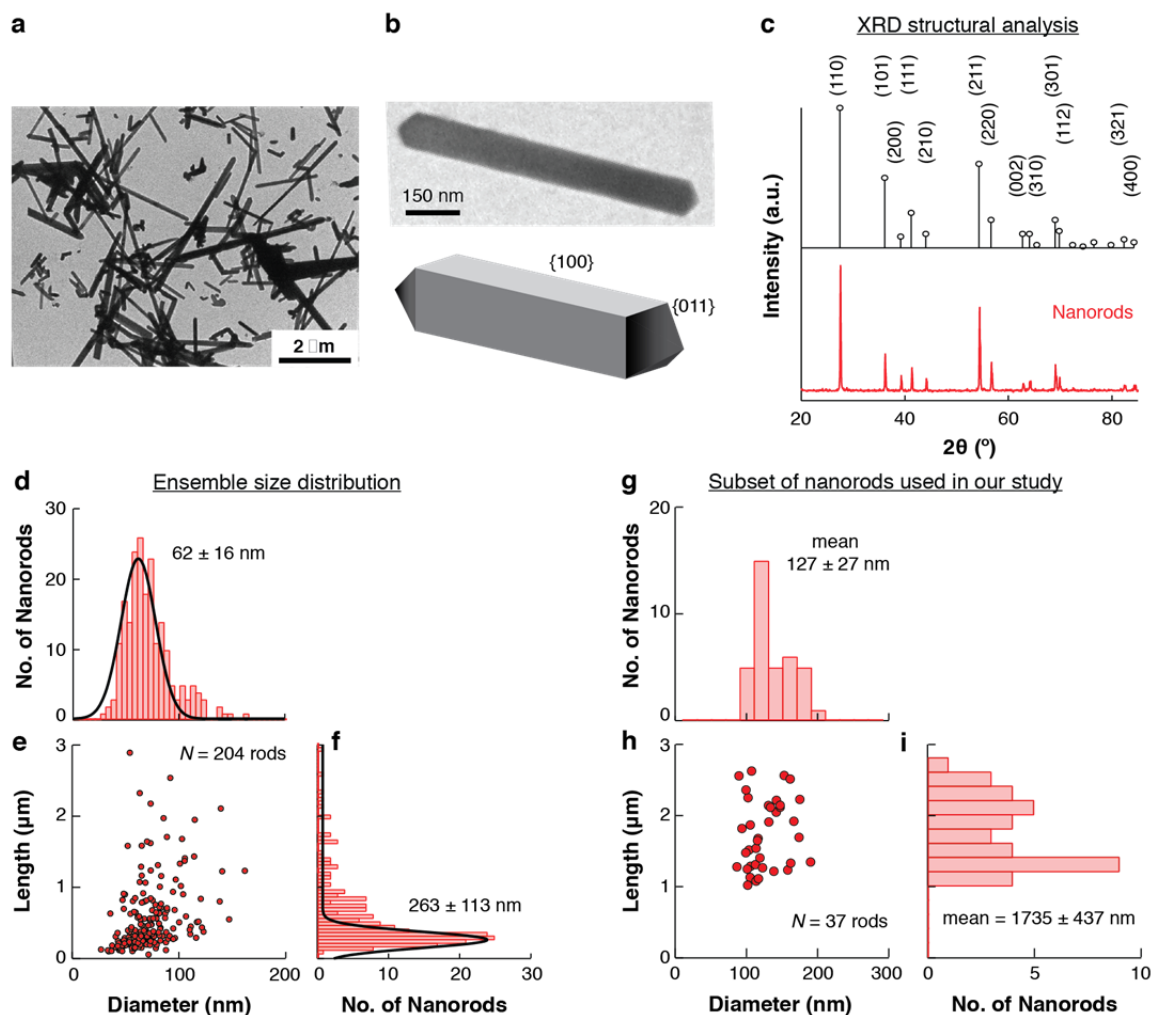
5.7. The OEC-derived photocurrent enhancement reliably reflects an enhancement in water oxidation rates, and is not due to larger photocurrent transient dynamics that might complicate our lock-in detected chopped-light measurements.	32
5.8. Nano-optical antenna effects change the absolute magnitudes of η , k_h , and k_e , but do not affect their correlations and their trends from which we draw our scientific conclusions.....	33
6. <u>Additional references</u>	36

SUPPLEMENTARY FIGURES and SUPPLEMENTARY NOTES

1. Supplemental figures and experimental methods

1.1. Characterization of TiO₂ nanorods.

Supplementary Figure 1 below summarizes the structural characterization results of TiO₂ nanorods.



Supplementary Figure 1 | Structural analysis of TiO₂ nanorod sample. **a**, Representative TEM image of the sample. The nanorods were synthesized in the absence of organic ligands, washed extensively following their synthesis and annealed at 450°C for 30 min on the ITO electrode prior to all measurements. **b**, TEM image of a single nanorod (top) and cartoon illustration (bottom) with surface facet assignments according to reference¹. **c**, XRD pattern of air annealed (450 °C for 30 min) TiO₂ nanorods (red) compared with a standard rutile TiO₂ XRD pattern (JCPDS 21-1276, black), demonstrating that these nanorods are rutile TiO₂. **d**, Distribution of diameters measured from 204 nanorods. The observation of a single population, with an average width of 62 ± 16 nm, suggests that the nanorod width is equal to the height, consistent with the original report that the nanorods have rectangular cross sections¹. **e**, Correlation plot of nanorod length versus diameter ($\rho = 0.40 \pm 0.04$), indicating that longer nanorods tend to have larger diameters. **f**, Distribution of nanorod lengths with a major population of nanorods exhibited an average length of 263 ± 113 nm. **g**, Distribution of diameters from the 37 nanorods used in the correlated single molecule imaging and *i-E* study (mean width = 127 nm, std = 27 nm, measured by SEM). **h**, Correlation plot of nanorod length versus diameter for the 37 nanorods. **i**, Distribution of nanorod lengths (mean length = 1735 nm, std = 437 nm).

1.2. Physical picture of the dual oxidation-reduction activity of high efficiency sites on bare TiO₂ nanorods for photoelectrochemical water oxidation.

To rationalize the correlated hole and electron surface activity, we hypothesized that this dual oxidation-reduction activity might facilitate high efficiency sites to accept photogenerated holes from the semiconductor interior and transfer them to adsorbed OH⁻ or H₂O (i.e., the sites are oxidized and reduced sequentially).

Supplementary Scheme 1 below illustrates the physical picture of our hypothesis. Under anodic conditions where our experiments were carried out, there is a net hole flux from the semiconductor interior to the

surface sites and subsequently to solution species (e.g., $\text{OH}^-/\text{H}_2\text{O}$) (black solid lines in Supplementary Scheme 1); at the same time, there is a net electron flux toward the ITO contact. When holes are transferred from the interior to surface sites, the surface sites get oxidized (i.e., site_{ox} ; note a “site” could be clusters of surface atoms); when the subsequent hole transfer to $\text{OH}^-/\text{H}_2\text{O}$ occurs, the surface sites get reduced (i.e., site_{red}). Therefore, during steady-state photoanodic water oxidation, the surface sites continuously undergo “redox-cycling”. Sites that can mediate water oxidation more efficiently are thus also expected to mediate both oxidation and reduction reactions more efficiently, i.e., dual oxidation-reduction activity.

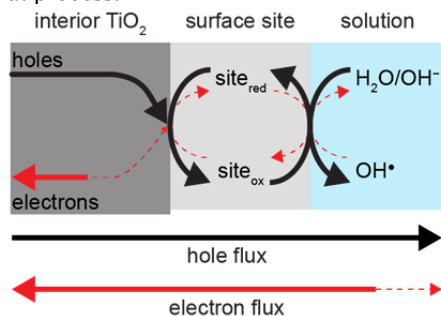
Even under overwhelmingly anodic conditions, some photogenerated electrons can also diffuse toward the surface and be captured by site_{ox} , generating site_{red} (dashed red lines in Supplementary Scheme 1), which can then transfer the electron to solution-phase acceptors (e.g., OH^\bullet , or our electron probe molecule Rz), giving the same “redox-cycling” as above (only in the reverse direction with respect to the electron flow direction). Therefore, the same higher efficiency sites that efficiently mediate the hole flux into solution would also perform better for mediating this minor electron flux into solution, giving rise to our observed correlated hole/electron activity.

Energetically, the dual oxidation-reduction activity could result from that these higher efficiency sites have their redox potentials poised in a range that facilitates both the oxidation and reduction halves of this “redox-cycling”. Externally, the applied potential controls the availability of surface-accessible holes and electrons (e.g., holes: Eq. S18 in SI Section 4.1; electrons: Eq. S28 in SI Section 4.2), which accounts for the observed hole- and electron-induced reaction rates having opposite potential dependences (Fig. 1n).

In summary, the higher hole and electron activity sites efficiently “redox-cycle” between oxidized and reduced states to generate oxidized products, but their ability to rapidly redox-cycle also makes them responsible for surface recombination when photogenerated electrons diffuse to the surface site.

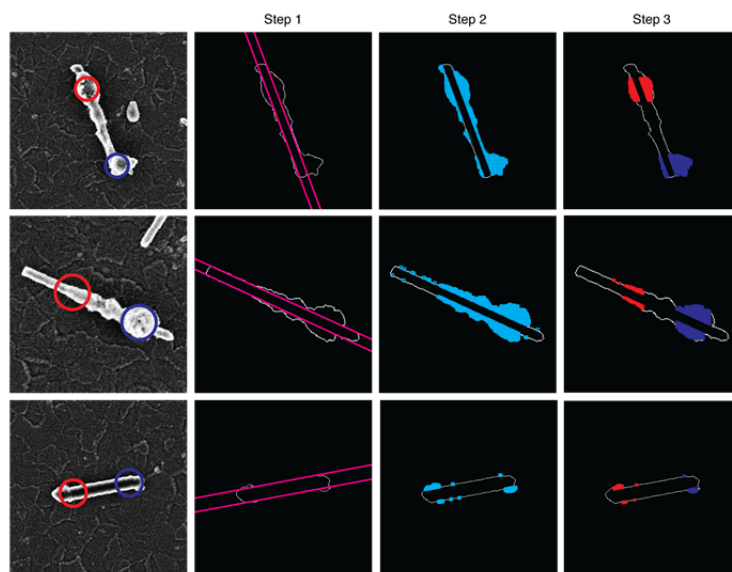
Our observed correlated hole/electron activities are consistent with the report by Rohrer et al that for micron-sized crystals of SrTiO_3 , both oxidative and reductive photocatalytic reactions prefer to occur on the $\{100\}$ facets (note their studies are at the facet level, whereas our correlated hole/electron activity is at the sub-facet level with nanometer resolution).

Supplementary Scheme 1 | Schematic of “redox-cycling” of surface active sites under photoanodic water oxidation conditions. Photogenerated holes are transferred from the semiconductor interior to surface sites (i.e., the sites get oxidized, site_{ox}); oxidized surface sites then transfer holes to (and accept electrons from) $\text{H}_2\text{O}/\text{OH}^-/\text{AR}$ (i.e., the sites get reduced, site_{red}). Some photogenerated electrons can also diffuse toward the surface, reducing site_{ox} to generate site_{red} , which can get oxidized via electron transfer to surface acceptors (e.g., OH^\bullet or Rz), giving the same redox-cycling of surface sites but opposite in direction in electron flow. The availability of surface accessible holes and electrons is controlled by the applied potential, giving rise to the observed potential-dependent hole- and electron-induced surface reaction rates (Fig. 1n). Here we neglect those holes that recombine with electrons in the depletion region as our single-molecule experiments do not probe that process.



1.3. Estimation of the deposited Co-B_i OEC amount by analyzing SEM images.

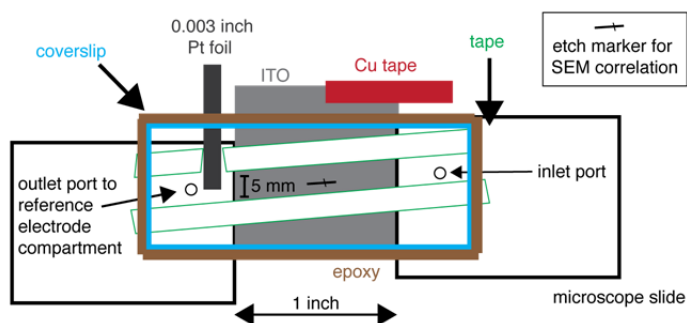
To estimate the amount of Co-B_i catalyst deposited using our localized photoelectrochemical deposition strategy, we developed an algorithm for analyzing SEM images. The procedure is illustrated in Supplementary Figure 2.



Supplementary Figure 2 | Estimating the Co-B₁ catalyst coverage on TiO₂ nanorods. Each row represents data from a single nanorod. Each column represents a step in the algorithm of catalyst quantification. Left column: SEM images of TiO₂ nanorods with deposited amorphous Co-B₁ catalysts. In step 1, we created a binary image from the SEM image and identified regions of the nanorod without catalyst by manual image inspection and knowledge of the laser focus position during photoelectrochemical deposition (circles in step 1). The bare nanorod boundaries are determined by fitting edge pixels at regions without catalyst (solid pink line). In step 2, all pixels outside the boundary are identified and filtered based on position to identify pixels within the focused laser spot (step 3). The areas of these pixels were used as a measure for the amount of catalyst deposited in units of μm^2 , as shown in Fig. 3c in the main text and Extended Data Figure 9c-d.

1.4. Electrochemical flow cell design.

Supplementary Figure 3 below shows a schematic of the 3-electrode electrochemical flow cell. This cell was mounted on the stage of an inverted optical microscope as in Fig. 1a of the main text.



** epoxy was also applied to back side to bond ITO and microscope slides

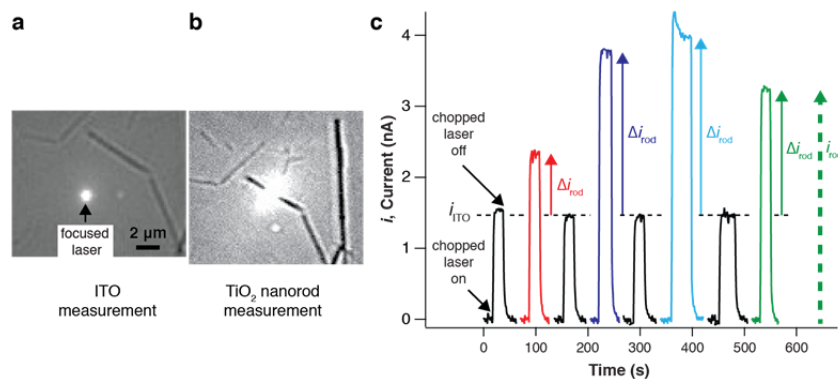
Supplementary Figure 3 | Schematic design of the 3-electrode electrochemical flow cell reactor. Polyethylene tubing (not shown) was inserted into the inlet and outlet ports and connected to a reservoir of N₂-purged reactant solution and the reference electrode compartment, respectively. All exposed edges and possible leak areas were sealed with Varian Torr Seal® epoxy.

1.5. Diffraction-limited sub-nanorod photocurrent measurements.

Supplementary Figure 4c shows a representative set of photocurrent versus time measurements at +0.2 V at different locations on the sample. When the continuously chopped, 8 mW focused 375 nm laser was positioned

on the ITO substrate (6.6 MW cm^{-2} ; Supplementary Figure 4a), a small, constant photocurrent signal was observed by the lock-in amplifier, indicated as i_{ITO} in Supplementary Figure 4c. It is worth noting that the ITO background current was not detectable over the potential range of $-0.7 < E < +0.2 \text{ V}$ using wide-field TIRF ($\sim 0.5 \text{ kW cm}^{-2}$) or unfocused ($\sim \text{mW cm}^{-2}$) illumination and the same lock-in detection method, presumably due to the low light power density of the 375 nm light. When the focused laser was placed on a nanorod (Supplementary Figure 4b), a nanorod-dependent photocurrent response was observed that was reproducibly and significantly larger than the ITO background current, indicated as i_{rod} by the dashed green arrow in Supplementary Figure 4c. In some cases, the nanorod photocurrent versus time response showed an instantaneous photocurrent spike when the modulating light pulse initially excited the nanorod. Single spot photocurrent measurements on individual nanorods were acquired when the photocurrent decayed to a steady state value, typically after 5-15 s (see Supplementary Figure 4c for ensemble-averaged photocurrent-time responses under chopped illumination). The single spot photocurrent versus potential data reported in the manuscript represents the difference (Δi_{rod}) between the individual nanorod photocurrent and the average of 10-15 individual ITO background measurements. Only those ITO background measurements that were within 5-10 μm from a single target nanorod were used for subtraction. The steady state photocurrent signal was averaged for 10 s and the error bars represent the standard deviation.

Our approach to measure photocurrent from a single nanorod under photoelectrochemical water oxidation conditions does not involve lithography steps to electrically contact individual nanorods, as is typically done in single nanorod photovoltaic measurements (which measures the current through solid-state electrical contacts made by high-resolution lithographical techniques rather than the current through the nanorod-solution interface we measure here)³⁻⁶, nor does it require a scanning probe⁷ to both locate nanorods and sensitively measure the photocurrent. To the best of our knowledge, this represents the first report of photoelectrochemical i - E measurements of single, isolated, nanomaterials without using scanning probes or lithographic electrical contacts. We note that the general approach of scanning optical photoelectrochemical microscopy was introduced in the 1980s to study microscopically-varying (i.e., micron scale) properties of semiconductor films⁸, specifically for TiO_2 films^{9,10}, but single-particle measurements were not reported.



Supplementary Figure 4 | Methodology of photocurrent measurements at a single spot on a single nanorod. a, The reflection of the 375 nm laser beam is visualized on the CCD camera for a typical ITO substrate background photocurrent measurement. The 375 nm laser was first collimated and expanded to fill the back aperture of the objective to achieve a tight focus. The FWHM of the reflection image of the focused laser was measured to be 392 nm, taken as the diameter of the laser focus. b, The focused laser beam was then positioned on a nanorod of interest to measure photocurrent at a selected spot. The laser spot reflection appears bigger in the image due to scattering by the nanorod. c, Representative photocurrent versus time data at +0.2 V acquired using lock-in detection at 1 Hz chopped laser illumination (50% duty cycle). The phase angle that maximized the in-phase photocurrent signal at +0.2 V was used for all potentials¹¹. The laser power was 8 mW focused to an area of $1.2 \times 10^{-9} \text{ cm}^2$, yielding a power density of 6.6 MW cm^{-2} . The black traces represent 4 individual ITO background measurements and the magnitude of the signal is indicated as i_{ITO} . The red, blue, teal and green traces represent photocurrent signals from 4 nanorod spots from 4 different nanorods. The dashed green arrow represents the magnitude of the photocurrent signal when the laser beam is positioned on the nanorod (i_{rod}). The horizontal dashed black line represents the average ITO substrate current response. The solid red, blue, teal and green arrows indicate the difference (Δi_{rod}) between the average ITO photocurrent and the steady state photocurrent from a single spot on a nanorod.

2. Detailed data analysis procedures after single-molecule super-resolution localization analysis of fluorescence images

2.1. Single-molecule fluorescence image analysis for super-resolution localization.

Identifying single molecules. The fluorescence images in the movies were analyzed using a home-written Matlab program, iQPALM (image-based quantitative photo-activated localization microscopy). The details of the program, including the image background subtraction routine, can be found elsewhere¹². Under our experimental conditions, the TiO₂ nanorods were not emissive over the wavelength range (550 nm to 610 nm) that the fluorescence signal of resorufin product molecules was collected. Each fluorescence image was background subtracted¹² and any pixel whose intensity value was greater than the mean pixel intensity plus 6 standard deviations was considered as a potential candidate molecule. This intensity threshold typically yielded <10 candidates per frame (each frame typically 15 × 50 μm²). Typically there were more than 50 TiO₂ particles/nanorods per frame, however only isolated nanorods (confirmed by SEM imaging) were selected for further analysis.

The centroid location of each product molecule was determined by fitting a 13 × 13 pixel area centered at the molecule's coordinate with a 2D Gaussian point spread function (PSF) (Eq. S1) where $I(x,y)$ is the EMCCD fluorescence intensity counts (*cts*) of the candidate at position x,y (nm) and A , B , (x_0,y_0) , and (σ_x,σ_y) are the amplitude, background, centroid location, and standard deviation of the fitted Gaussian function, respectively.

$$I(x,y) = A \exp \left[-\frac{(x-x_0)^2}{2\sigma_x^2} - \frac{(y-y_0)^2}{2\sigma_y^2} \right] + B \quad \text{Eq. S1}$$

The total integrated volume under the 2D Gaussian was converted to the total number of fluorescence photons (N) via Eq. S2 according to the camera supplier (Andor Technology), where g , S , and QE are the EM gain (unitless), sensitivity (electrons per count), and quantum yield (unitless) of the EMCCD camera in the spectral range of detected fluorescence, respectively. The 3.65 physical constant (eV per electron) accounts for electron creation in silicon and E_{hv} (in eV) is the energy of a single fluorescence photon from resorufin with an emission maximum wavelength at 585 nm or $E_{hv} = 2.12$ eV.

$$N = \frac{\left(\frac{cts}{g}\right) \times \left(\frac{S}{QE}\right) \times 3.65}{E_{hv}} \quad \text{Eq. S2}$$

The localization error (Err_i , $i = x$ or y) of the product molecule centroid position was estimated according to Eq. S3^{13,14}

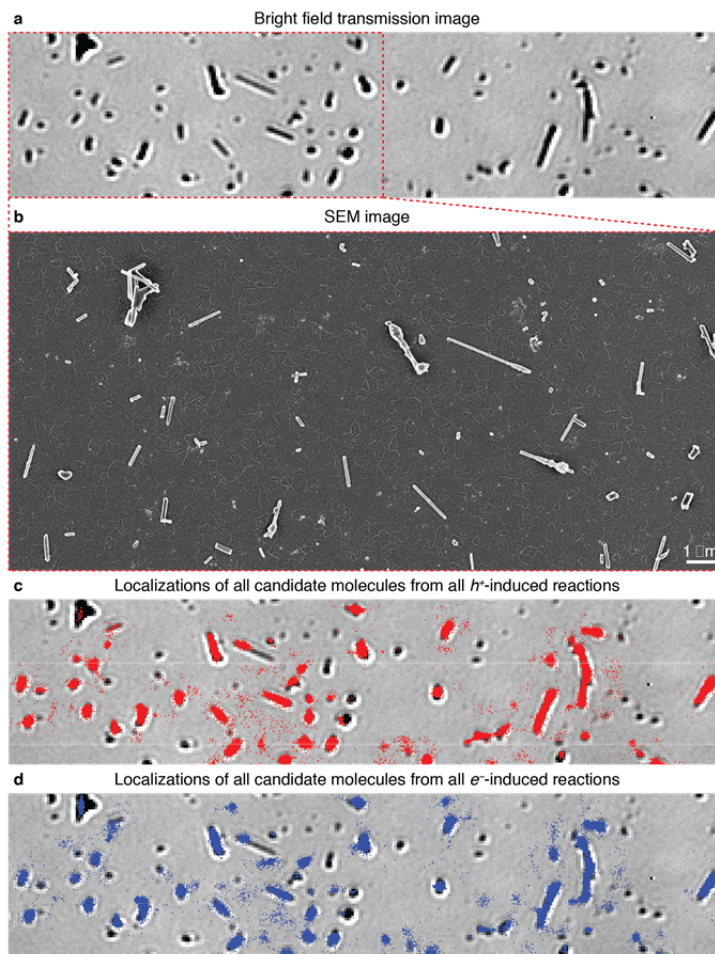
$$Err_i = \sqrt{\frac{\sigma_i^2}{N} + \frac{a_i^2}{12N} + \frac{8\pi\sigma_i^2 b^2}{a_i^2 N^2}} \quad \text{Eq. S3}$$

where a_i is the pixel size; b is the standard deviation of the background fluorescence image according to reference¹². Extended Data Fig. 5a shows the distribution of the localization error for all product molecules generated on a representative single nanorod.

The localizations of individual product molecules were further filtered to remove candidates whose PSF widths were either too small or too large to represent single product molecules and corrected for cases when a product molecule adsorbed on the nanorod surface for multiple frames or when a single frame can contain multiple unresolved molecules within a diffraction-limited resolution on the same nanorod; these additional data analysis details are presented in Sections 2.2 and 2.3 below.

Correct for stage drift. The sample drift was monitored in a frame-by-frame fashion by fitting the emission from individual 100 nm Au nanoparticle fluorescent markers adsorbed on the ITO electrode. The average drift of 3 to 5 Au markers per frame was used to correct the centroid position of each candidate molecule.

Identifying regions of interest (ROIs). The bright field optical transmission image of a nanorod-coated ITO electrode is shown in Supplementary Figure 5a. The localized positions of all candidate molecules detected at all potentials during photoelectrochemical oxidation of AR (red dots in Supplementary Figure 5c) and photoelectrochemical reduction of Rz (blue dots in Supplementary Figure 5d) were overlaid on the transmission image and it was immediately apparent that all of the candidates spatially overlapped with the TiO₂ particles on the ITO substrate. Although approximately 20-40 TiO₂ particles could be identified per optical field of view, only well-isolated, non-aggregated nanorods visualized by SEM imaging (Supplementary Figure 5b) were selected as ROIs. A list of ROIs was generated by thresholding the transmission image to identify dark contrast objects in Supplementary Figure 5a and dilating each ROI by 1 pixel.



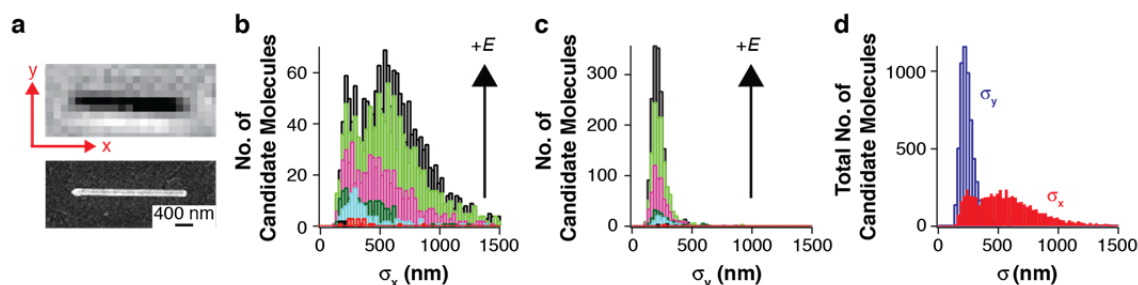
Supplementary Figure 5 | Overlay of all candidate fits of individual product locations on bright field transmission images. a, Bright field transmission image of nanorod sample on ITO. b, Corresponding SEM image of the sample region indicated by the dashed red box in a that is used to determine the structure of individual nanorods. c-d, Overlay of all candidates of individual product locations on the transmission image detected during photoelectrochemical oxidation of AR (c) and reduction of Rz (d).

Generating super-resolution reaction images. The eventual map of product localizations such as those in Supplementary Figure 5c-d can be plotted as a scatter plot (as in Fig. 1b left in the main text, where each dot represents a single product molecule), which can be further histogrammed in a 2-D image format (as in Fig. 1b, right), where the color of each image pixel represents the number of product molecules detected at that location. This 2-D histogram image has super-optical resolution, as the original product locations were determined to ~30 nm precision.

The reaction rate at any location on a nanorod can then be obtained by counting the number of products per surface area and per unit time as a function of applied electrode potential.

2.2. Filtering candidate molecules by their PSF width and quantitative single-molecule counting algorithm.

Here we provide detailed descriptions of subsequent procedures used to remove noise contributions and spurious detections, correct for unresolved multiple-molecule detection or a product molecule adsorbed on the nanorod for multiple image frames. We analyzed the distribution of σ_x and σ_y from 2D Gaussian PSF fitting of candidates for each ROI. Supplementary Figure 6b and Supplementary Figure 6c show the distributions of σ_x and σ_y of fitted candidates for AR oxidation to P as a function of potential for a single nanorod oriented along the x -direction of the camera image (Supplementary Figure 6a). A population of candidates with σ_x and σ_y less than 100 nm was observed but we immediately rejected them because they are representative of a ‘hot’ pixel and the fitted PSFs are too narrow for a single molecule (the diffraction-limited width of a single-molecule PSF should be approximately $0.61 \times \lambda / \text{NA} = 585 \text{ nm} / (2 \times 1.2) = 297 \text{ nm}$, corresponding to $\sigma_{x,y} \sim 126 \text{ nm}$)¹⁵.



Supplementary Figure 6 | Candidate molecule fit widths from a single TiO₂ nanorod. **a**, Bright field transmission image (top) and corresponding SEM image (bottom) of a single nanorod. **b-c**, Distributions of σ_x and σ_y for all candidate molecule fits at different potentials along the image x direction (**b**) and y direction (**c**). Different colors represent histograms at different potentials. **d**, Distribution of σ_x and σ_y for all candidates over all potentials along each image direction.

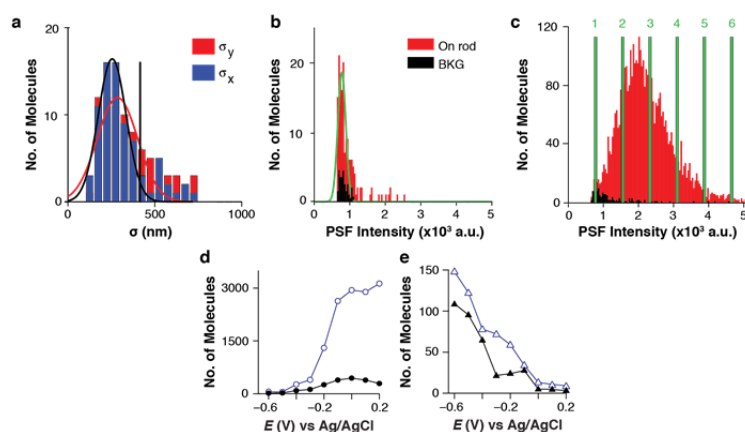
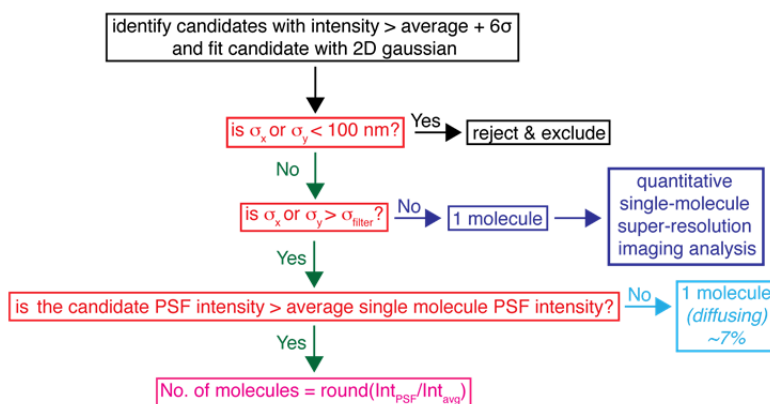
Supplementary Figure 6b shows a growing population of candidate molecules with $\sigma_x > 500 \text{ nm}$ as the potential was increased from -0.6 V to $+0.2 \text{ V}$, whereas a single population with an average $\sigma = 206 \text{ nm} \pm 65.5 \text{ nm}$ was observed in the y -direction (Supplementary Figure 6c and Supplementary Figure 6d). Therefore, the PSF fit width transversal to the nanorod long axis was not affected by increasing anodic potential whereas the PSF fit width along the nanorod long axis was significantly increased. This behavior can be attributed to the presence of multiple product molecules in each image frame on a single nanorod. This occurs at more positive potentials because there is a larger hole flux to the nanorod surface which accelerates the AR oxidation rates. When multiple P molecules are generated on the same nanorod, and the distance between them is larger than the diffraction limited spatial resolution, their individual center positions can be independently determined. However, if the distance between multiple P molecules is within the diffraction-limited resolution (here $\sim 300\text{--}400 \text{ nm}$), their fluorescence images would overlap heavily, leading to a broadened σ fit result. For the nanorod shown in Supplementary Figure 6a, the σ broadening is anisotropic because the molecules cannot separate by more than the nanorod width ($\sim 127 \text{ nm}$), which is much smaller than the diffraction-limited resolution, and thus would not cause broadening of the fitted PSF width (in this specific case along the y -direction). The simultaneous presence of spatially-unresolved multiple molecules also leads to an increase of the detected fluorescence signal counts per PSF fitting, which can be used to determine the number of molecules present on the nanorod surface (see below).

Another possibility for the increase in the fitted PSF width with increasingly positive potential is that the fluorescent product molecule has diffused on the nanorod surface within the image frame time (15 ms), leading to the broadening. This possibility is insignificant (see below) and its contribution to the potential dependence can be ruled out because the diffusion of P molecules is not expected to be strongly potential dependent. In addition, we observed σ broadening from two independent probe reactions at opposite potential regimes; σ broadening from AR oxidation occurred over the potential range $E = -0.3 \text{ V}$ to $+0.2 \text{ V}$, whereas for Rz reduction σ broadening occurred from $E = -0.3 \text{ V}$ to -0.6 V . Thus, the broadening is related to the potential-dependent reactivity rather than P diffusion. Furthermore, if the broadening was due to surface diffusion of P molecules, the increase in σ should not be accompanied by an increase of fluorescence intensity. However, we indeed observed a positive correlation between σ_x and PSF intensity. For example, the Pearson cross-correlation coefficient ρ between σ_x and PSF intensity for the nanorod in Supplementary Figure 6 was 0.55 ± 0.01 , where the error in ρ is given as

$0.6745(1 - \rho^2) / \sqrt{N}$, where N is the number of measurements¹⁶. Thus, the potential-dependent σ broadening and concomitant increase in PSF intensity is indicative of multiple P molecules separated by a distance less than the diffraction-limited resolution on a single nanorod.

In order to take into account the case of unresolved multiple molecules in a single image that broadens the fitted PSF width (e.g., σ_x and σ_y), we developed an algorithm, schematically shown in Supplementary Scheme 2, to quantitatively determine the number of product molecules generated per frame per nanorod. First, we identified a low reactivity potential range, -0.6 V to -0.4 V for AR oxidation and -0.2 V to $+0.2$ V for RZ reduction, where candidate fits *generally* exhibited a single population of σ_x and σ_y , which is indicative of a single-molecule imaging condition. In this low reactivity potential regime, we fit the distribution of σ_x and σ_y of every candidate with a Gaussian function and defined a σ_{filter} , which is equal to the smaller value of average σ_x or σ_y value plus 2 standard deviations (σ_{filter} indicated as a bar in Supplementary Figure 7A). The σ_{filter} is the maximum allowable σ_x and σ_y for a single molecule. Candidates whose σ_x and $\sigma_y < \sigma_{filter}$ were classified as single molecules and included in later single-molecule super-resolution imaging analysis.

Supplementary Scheme 2 | Flow chart of the algorithm used to quantitatively count single product molecules



Supplementary Figure 7 | **Quantitative single-molecule counting data analysis procedure using AR photoelectrooxidation data as an example.** a, Determination of the σ_{filter} by fitting the distributions of candidate σ_i with a Gaussian function in the low reactivity potential range (-0.6 V to -0.4 V). The σ_{filter} was defined as the smaller value of either average σ_x or average σ_y plus 2 standard deviations (indicated by vertical bar). These data are part of those in Supplementary Figure 6. b, Distribution of integrated intensities per frame of the single molecule candidates in the low reactivity potential range (-0.6 V to -0.4 V), and the fit with a Gaussian function to determine the average integrated intensity of a single product molecule (Int_{avg}). c, Same as (d), but for all candidates detected over all potentials. For the image frame that contains more than one molecule, the number of molecules was determined by dividing the intensity of the

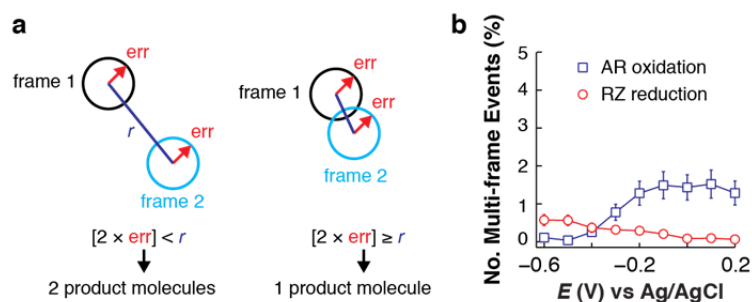
candidate PSF by the average intensity of a single molecule, Int_{PSF}/Int_{avg} , and rounding to the nearest integer. The green bars represent the integrated intensity values for various numbers of molecules. d-e, Corrected (purple lines, open symbols) and original (black lines, closed symbols) number of molecules detected at each potential for AR photoelectrochemical oxidation (d) and Rz photoelectrochemical reduction (e) in one fluorescence catalytic movie.

To account for multiple molecules generated per frame, or single product molecules that diffuse on the surface during the single frame acquisition time, the integrated intensity of the 2D Gaussian PSF was analyzed. The distribution of integrated PSF intensities in the low reactivity potential regime was fit with a Gaussian function (Supplementary Figure 7b) to determine the average value for a single molecule (Int_{avg}). For candidates with σ_x or $\sigma_y > \sigma_{filter}$, the number of molecules generated per frame was determined by dividing the individual candidate PSF intensity by the average intensity of a single product molecule, Int_{PSF}/Int_{avg} , and rounding to the nearest integer (Supplementary Figure 7c). Candidates with Int_{PSF} representative of a single molecule but did not satisfy the requirement that σ_x and $\sigma_y < \sigma_{filter}$ were considered as P molecules that diffused on the TiO_2 surface during the image frame time. In the low reactivity potential regimes for AR oxidation and Rz reduction, only $9 \pm 6\%$ and $5 \pm 4\%$ (i.e., on average $\sim 7\%$; data averaged over 12 nanorods) of candidates were classified as single, diffusing P molecules, respectively, and they were not included in constructing the super-resolution reactivity images.

Single-molecule blinking is insignificant in our measurements. We previously determined that the average single-molecule photoblinking on-time of resorufin (product molecule in our study) was ~ 5 s under 130 W/cm^2 532 nm laser illumination¹⁷. The 532 nm laser power density used in this study was $\sim 5 \times$ greater (630 W/cm^2). As photoblinking rate typically scales linearly with laser power density, the expected average photoblinking on-time here would be ~ 1 s, much longer than the observed average product residence time of ~ 0.015 s (Extended Data Fig. 7c, f, i, and j). Therefore, single-molecule blinking is insignificant in the measurements here.

2.3. Correcting for single product molecules adsorbed on the surface for more than one frame.

We also considered the possibility that a single product molecule, with σ_x and $\sigma_y < \sigma_{filter}$, could be adsorbed on the TiO_2 nanorod surface for a time longer than a single frame acquisition time (15 ms). This effect, termed a multi-frame event, could lead to an overestimation of catalytic activity if the same product molecule is counted multiple times. We used an algorithm, schematically shown in Supplementary Figure 8a, to quantitatively count single product molecules detected in consecutive frames on the same nanorod. If two molecules were detected in consecutive frames, we considered each molecule to be two, individual, product molecules (from two separate catalytic reactions) if the distance between the localized center positions is greater than two times of the location error (err) in each molecule's 2D Gaussian PSF fit (Supplementary Figure 8a, left). The err was calculated by $err = \sqrt{Err_x^2 + Err_y^2}$, where the average Err_x and Err_y for all detected single molecules is approximately 32 nm (Extended Data Fig. 5a). However, if two single molecules were detected in consecutive frames and the distance between their center positions in the two frames was less than $2 \times err$ (Supplementary Figure 8a, right), they are counted once and the center position of the molecule in the first of the two frames is used to plot its position in super-resolution reaction maps.



Supplementary Figure 8 | Quantitative counting of product molecules detected in multiple frames. a, Schematic illustration of algorithm used to determine if single product molecules detected in consecutive frames are considered to be

different product molecules (left) or the same product molecule (right). **b**, Percentage of single product molecules that are detected in more than 1 frame. The data here are pooled from 37 nanorods and the error bars are SEM.

Supplementary Figure 8b shows that, in the low reactivity potential regimes for AR oxidation (-0.6 V to -0.4 V) and Rz reduction (-0.2 to $+0.2$ V), $>98\%$ of product molecules are only detected for a single frame. The number of multi-frame events increases as the reactivity increases (in opposite potential directions for the two reactions). This is most likely not due to a potential-dependent product adsorption time because the same product molecule detected in the low reactivity potential regimes for both reactions was observed to have short adsorption time. Alternatively, the slight increase in multi-frame events versus potential is likely due to the generation of two individual product molecules at the same nanorod location in two consecutive frames. Regardless, the percentage of single molecules that are detected in multiple frames is less than 3% overall and plays an insignificant role in quantitative single molecule counting.

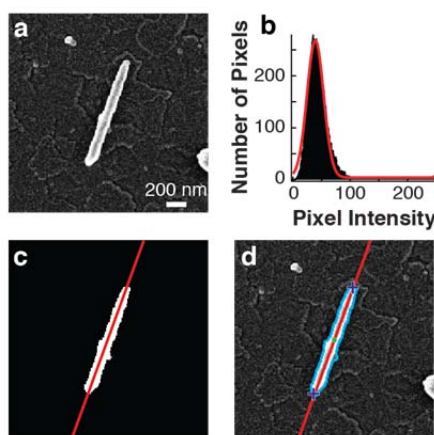
Supplementary Figure 7d-e shows representative results before and after correcting for (i) one fluorescence image may contain multiple spatially unresolved molecules, which occurs frequently in the high reactivity potential range and (ii) one molecule may adsorb on the nanorod surface for more than one frame, which does not occur significantly across all potentials. For the AR oxidation reaction in the high reactivity potential regime (-0.3 V to $+0.2$ V), the total number of product molecules generated was typically $3\times$ to $8\times$ larger after correction. The effect of multiple product molecules imaged per frame was less important for the Rz reduction reaction, where the total number of product molecules after correction was merely $<2\times$ larger. This smaller difference for Rz reaction results from the overall lower number of reductive reactions while the electrode acts as a photoanode.

2.4. Mapping the nanorod structural contour from SEM onto the super resolution single-molecule reaction images.

Single molecule imaging experiments were performed on a region of the sample near a macroscopic position marker (e.g., scratches made by a diamond scribe), which facilitated the direct correlation between SEM and optical images. In this section, we describe the strategy to map the SEM structure contour of nanorods onto the super-resolution single-molecule imaging data.

2.4.1. Determining the nanorod center position and contour from SEM images.

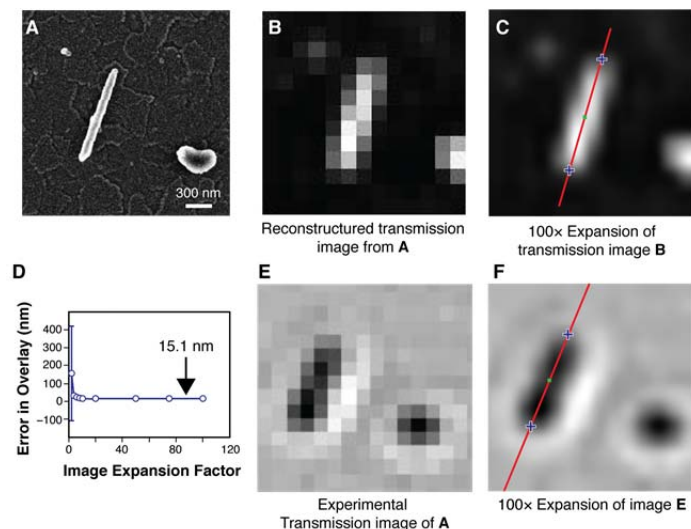
Supplementary Figure 9 shows the image processing routine used to determine the center positions of individual nanorods in SEM images.



Supplementary Figure 9 | Determine the center positions of individual nanorods in SEM images. **a**, Representative SEM image of a single TiO_2 nanorod. **b**, Gaussian fit to the distribution of pixel intensities to determine the image threshold (average $+ 2\sigma$; σ = standard deviation of the Gaussian fit). **c**, Binary image created from thresholding the image and removing any small, residual objects based on area of object, for example the small, high contrast object in the top left of **(a)**. The red line is the linear least squares fit result to the binary image. **d**, Linear least squares fit result to the binary image (red line) overlaid on the original SEM image. The nanorod contour pixels are represented by light blue. The center position of the rod (green dot) was determined as the midpoint of the line profile from the nanorod ends (blue crosses).

2.4.2. Estimating error 1: the error in overlaying nanorod center positions from reconstructed optical transmission images is 15 nm.

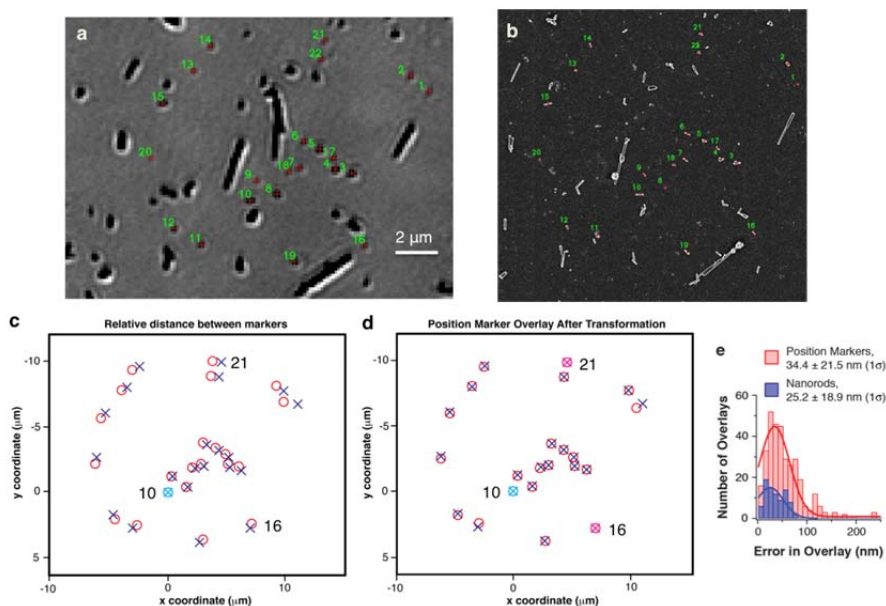
We used the same linear least squares fitting methodology as described in Supplementary Figure 9 to determine the center position of nanorods from bright field transmission images.



Supplementary Figure 10 | Determination of center position of nanorods in reconstructed and experimental bright field transmission images. a, Representative SEM image of a nanorod. b, Reconstructed optical transmission image of (b) by convoluting (a) with a Gaussian function with FWHM = 297 nm, corresponding to the ideal diffraction-limited PSF, and increasing the pixel size to 155 nm to match our optical image pixel size. c, The image in (b) was expanded 100× using bicubic interpolation, thresholded to create a binary, and the linear least squares fitting routine was used to identify the center position (green dot) of the nanorod as in Supplementary Figure 9d. We computed the error as the separation between the center position determined from the original SEM image as in Supplementary Figure 9d and that from the reconstructed optical transmission image as in (c). d, The error in overlaying the center positions of 8 nanorods from reconstructed optical transmission image onto the center positions determined from their original SEM images as a function of image expansion factor. The error in the computed center positions decreased as the image expansion factor increased, and eventually reached a limiting value of ~15 nm, which we estimate as the error in our method in overlaying the center positions from reconstructed optical images to SEM images. e, Experimental optical transmission image of the same nanorod in (a). f, Determination of the center position of nanorod in (e) using 100× image expansion.

2.4.3. Estimating error 2: error in overlaying nanorod center positions from experimental images using position markers.

We then performed the same routine described in Supplementary Figure 10a-c on experimentally measured optical transmission images (Supplementary Figure 10e). The transmission image was expanded 100× using bicubic interpolation, thresholded to create a binary image, and the center position of the rod was determined by using a linear least squares fit to the expanded image (Supplementary Figure 10f). Supplementary Figure 11 shows how we estimated the error in overlaying the center positions of nanorods determined in both images.



Supplementary Figure 11 | Error in overlaying position markers in SEM and bright field optical transmission images.

a, Bright field optical transmission image where the red crosses indicate the center positions of diffraction-limited particle-like objects (position markers) determined by a 2D Gaussian fit. **b**, SEM image of the same sample area where the red crosses indicate the center positions of the same markers in **(a)**. **c**, Scatter plot of the markers when the same common origin is used (marker 10). Blue crosses and red open circles represent optical transmission and SEM center positions, respectively. **d**, Using markers 16 and 21, we computed the transformation matrix to rotate and scale the marker coordinates to account for image distortion. We repeated this process multiple times for different images and marker combinations to estimate the error in overlaying the center positions of objects. **e**, Distribution of the error in position marker and nanorod center position overlay between optical transmission images and SEM images. The average value of overlaying nanorod center positions is 10 nm smaller than the error in overlaying position markers, which we attribute to the 1D nature of the nanorod compared to some of the irregularly shaped diffraction-limited objects in **a** with a 2D Gaussian fit (e.g., particles 10, 15 and 19 in **b**). Most important, the nanorod contour determined from SEM images could be accurately mapped onto the center position of nanorods determined from optical transmission images with 25 nm precision.

3. Analysis of i - E data with the Gärtner-Butler model

A general expression for the photocurrent at a semiconductor-liquid junction is $i = I_{\text{abs}} \times \eta_{\text{sep}} \times \eta_{\text{surf}}$, where I_{abs} refers to the number of absorbed photons (s^{-1}), η_{sep} is the efficiency of charge-carrier separation and transport to the collecting contacts and η_{surf} is the efficiency of charge transfer at the interface¹⁸. We experimentally observed that i is proportional to I_0 and $(E)^{1/2}$ at positive potentials. The Gärtner model theoretically predicts the observed behavior.

3.1. Introduction to the Gärtner Model

In 1959, Gärtner introduced the so-called depletion approximation to calculate the photocurrent density J (A cm^{-2}) for an illuminated solid-state p - n junction¹⁹. Later, Butler applied this theory to an illuminated semiconductor-liquid junction and quantitatively described the J - E data of a single crystal bulk WO_3 electrode during the photoelectrolysis of water²⁰. The Gärtner-Butler model assumes the following (refer to Supplementary Scheme 3a for the coordinate system)^{21,22}:

1) Every absorbed photon produces an electron-hole pair. I_{abs} as a function of distance into the semiconductor x follows the Beer-Lambert law.

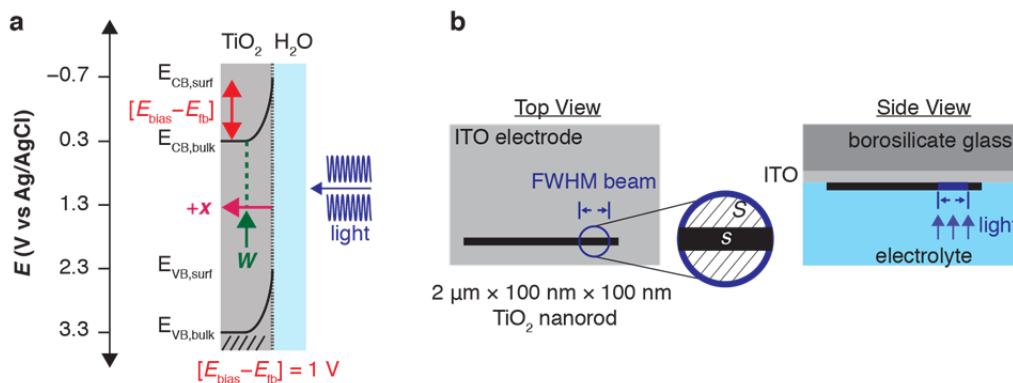
2) All changes in potential are entirely manifested as a potential drop within the depletion region (W) of the semiconductor. Supplementary Scheme 3a shows a schematic illustration of an n -type TiO_2 sample in aqueous electrolyte for E more positive than the semiconductor flat band potential (E_{fb}) (e.g., by 1 V in Supplementary Scheme 3a). At this condition, the so-called band bending effect takes place, where the conduction and valence

band edge potentials at the surface ($E_{CB,surf}$ and $E_{VB,surf}$) differ from the conduction and valence band potentials in the bulk ($E_{CB,bulk}$ and $E_{VB,bulk}$) by $(E - E_{fb}) = 1$ V.

3) Carriers generated within the depletion region (e.g., for any $x \leq W$ in Supplementary Scheme 3a) are collected with unity efficiency; i.e., $\eta_{sep} = \eta_{surf} = 1$ for carriers located at a distance $x \leq W$.

4) Carriers generated outside the depletion region (i.e., $x > W$) can be collected if they diffuse to the depletion layer edge.

Supplementary Scheme 3 | a, Schematic illustration of the coordinate system of light penetration (x) relative to the width of the depletion region (W) for $(E - E_{fb}) = 1$ V for an n -type TiO_2 photoelectrode. **b**, Experimental configuration for single nanorod photocurrent measurements. A spot of a single nanorod with geometric cross sectional area s is illuminated with a focused laser with a geometric cross section S .



3.2. Gärtner model for an n -type photoelectrode with minimal light absorption within W and negligible photocurrent contribution from carriers generated for $x > W$.

In this section we derive an expression to fit i - E data of single nanorods using an adapted form of the Gärtner model, as was originally used by Butler²⁰, but modified to take into account our illumination geometry.

3.2.1. Gärtner model for bulk semiconductor electrodes.

Gärtner's expression for the total current density J_{tot} (A cm^{-2}) is given by

$$J_{tot} = -q\Phi_0 \left(1 - \frac{\exp(-\alpha W)}{1 + \alpha L_p} \right) - qp_0 \frac{D_p}{L_p} \quad \text{Eq. S4}$$

where q ($= 1.60218 \times 10^{-19}$ C) is the electronic charge, Φ_0 is the incident light power density ($\text{s}^{-1} \text{cm}^{-2}$), α is the monochromatic linear absorption coefficient (cm^{-1}), L_p is the hole diffusion length (cm), p_0 is the equilibrium hole concentration in the dark (cm^{-3}), D_p is the diffusion coefficient of holes ($\text{cm}^2 \text{s}^{-1}$) and W is the depletion layer thickness given by²²

$$W(\text{cm}) = \sqrt{\frac{2\epsilon\epsilon_0(E - E_{fb})}{qN_d}} \quad \text{Eq. S5}$$

where ϵ is the relative dielectric constant of TiO_2 ($= 100$ ²³), ϵ_0 is the permittivity of vacuum ($= 8.85419 \times 10^{-14}$ F cm^{-1}), E is the applied electrochemical potential (in V relative to the Ag/AgCl reference electrode), N_d is the doping density (cm^{-3}), and E_{fb} is the flat band potential (in V relative to the Ag/AgCl reference electrode). As the flat band potential is traditionally measured by capacitance measurements under dark conditions²⁴, and the photocurrent onset potential must be measured under illumination, we replace the term E_{fb} in Eq. S5 with the term $E_{on,GB}$ to avoid confusion (see discussions in Section 3.5 below). $E_{on,GB}$ here represents the photocurrent onset potential predicted by the Gärtner-Butler model.

The second term in Eq. S4 is typically considered negligible for wide band gap (E_g) semiconductors because the magnitude of $\left(qp_0 \frac{D_p}{L_p}\right)$ is many orders of magnitude smaller than $q\Phi_0 \left(1 - \frac{\exp(-\alpha W)}{1 + \alpha L_p}\right)$, which is equal to the hole flux to the semiconductor surface under illumination. Neglecting the $\left(qp_0 \frac{D_p}{L_p}\right)$ term in Eq. S4 gives Eq. S6:

$$J_{\text{tot}} = -q\Phi_0 \left(1 - \frac{\exp(-\alpha W)}{1 + \alpha L_p}\right) \quad \text{Eq. S6}$$

3.2.2. The magnitude of αL_p is $\ll 1$.

The contribution to J_{tot} from the electric-field free region depends on the amount of light absorbed within a diffusion length beyond W into the semiconductor, e.g., $\alpha_{375\text{ nm}} \times L_p$. Using the reported values of $\alpha_{375\text{ nm}} = 10^4\text{ cm}^{-1}$ ²⁵ and $L_p = 20$ to 30 nm for TiO_2 nanorods^{23,26}, $\alpha \times L_p = 0.03$, which is less than 5%. Therefore, Eq. S6 can be further simplified to:

$$J_{\text{tot}} = -q\Phi_0 [1 - \exp(-\alpha W)] \quad \text{Eq. S7}$$

Thus the total photocurrent becomes proportional to the photocurrent from carriers generated within W (J_{DL} , the photocurrent density from the depletion region):

$$J_{\text{tot}} = -q\Phi_0 [1 - \exp(-\alpha W)] = J_{\text{DL}} \quad \text{Eq. S8}$$

3.2.3. Expansion of the exponential term for $\alpha W \ll 1$.

In Butler's seminal report²⁰, he recognized that for long wavelength illumination (low values of α), $\alpha W \ll 1$, warranting expansion of the exponential term in Eq. S8. For example, for a nanorod with $N_d = 10^{18}\text{ cm}^{-3}$ and $E - E_{\text{fb}} = 0.9\text{ V}$, $W = 100\text{ nm}$ and $\alpha W = 0.1$. The exponential term in equation Eq. S8 can be expanded in a Taylor series and the higher order terms can be neglected. Eq. S8 becomes:

$$J_{\text{tot}} = -q\Phi_0 [1 - \exp(-\alpha W)] = -q\Phi_0 \left[1 - 1 + \left(\frac{\alpha W}{1!}\right)\right] = -q\Phi_0 \alpha W \quad \text{Eq. S9}$$

3.2.4. Positive sign convention for anodic photocurrent.

Gärtner's original derivation described the current density-potential (J - E) response for an illuminated solid-state p - n junction. The photocurrent density was expressed as a negative quantity. Later, Butler expressed the anodic photocurrent density generated at an illuminated wide band gap n -type photoelectrode in aqueous electrolyte (same as studied here) as a positive quantity²⁰. We will also express the anodic photocurrent as a positive quantity. We also multiplied Eq. S9 by the area where the light illuminates the sample, so that the equation Eq. S9 is expressed as a photocurrent i (A) (rather than current density J (A cm^{-2})) that depends on the incident light power I_0 (s^{-1}) (rather than light power density Φ_0 ($\text{s}^{-1}\text{ cm}^{-2}$)):

$$i_{\text{tot}} = qI_0 \alpha W = qI_0 \alpha \sqrt{\frac{2\epsilon\epsilon_0(E - E_{\text{fb}})}{qN_d}} \quad \text{Eq. S10}$$

3.3. Light absorption of an individual rutile TiO_2 nanorod under focused laser excitation.

Supplementary Scheme 3b illustrates the illumination geometry for our single spot i - E measurements on single nanorods. For all nanorods studied herein, the geometric cross section of the nanorod (s) is smaller than the geometric cross section of the focused laser spot (S). To account for the light absorbed with the depletion region ($I_{\text{abs},W}$) of single nanorods in our illumination geometry, we modify Eq. S10 to

$$i_{\text{tot}} = qI_0\alpha\left(\frac{s}{S}\right)\sqrt{\frac{2\varepsilon\varepsilon_0(E-E_{\text{fb}})}{qN_d}} = qI_{\text{abs},W} \quad \text{Eq. S11}$$

The nano-optical effect of the nanorod is considered later in Section 5.8.

3.4. η is the absorbed photon to current efficiency within the depletion layer and it also characterizes the local photocurrent efficiency at a nanorod spot.

We previously discussed that the Gärtner model assumes $\eta_{\text{sep}} = \eta_{\text{surf}} = 1$ for carriers generated within W . This assumption is often unsatisfied for real semiconductor-liquid junctions. In order to quantify the efficiency of individual semiconductor nanorods from experimental i - E data, we introduce a photocurrent efficiency term η into Eq. S11, which represents the absorbed photon to current efficiency within the depletion layer of the semiconductor. η contains contributions from both η_{sep} and η_{surf} . Similar efficiency terms have been used to quantify the current efficiency of semiconductor electrodes^{27,28}.

$$i = \eta qI_0\alpha\left(\frac{s}{S}\right)W = \eta qI_0\alpha\left(\frac{s}{S}\right)\sqrt{\frac{2\varepsilon\varepsilon_0(E-E_{\text{fb}})}{qN_d}} \quad \text{Eq. S12}$$

3.5. Flat band potential is traditionally measured under dark conditions²⁴, while our measurements are performed under illumination, so we replace E_{fb} with $E_{\text{on,GB}}$, the photocurrent onset potential predicted by the Gärtner-Butler model.

The Gärtner-Butler model assumes that the electric field within the depletion region (and therefore the depletion region thickness W) is not affected by illumination (i.e., the model does not distinguish between dark and light conditions). Eq. S12 derived from the model predicts that the measured photocurrent onsets at the flat band potential (i.e., according to Eq. S12 when $E > E_{\text{fb}}$, $i > 0$). This ideal behavior has been observed for photoelectrochemical water oxidation using bulk rutile TiO₂ photoanodes²⁹. Alternatively, it has also been observed that the photocurrent onset potential for water oxidation using bulk rutile photoanodes is more positive (e.g., 0.1 to 0.5 V) than the flat band potential determined by Mott-Schottky analysis under dark conditions³⁰⁻³². We also experimentally observed a +200 mV difference between the flat band potential from Gärtner-Butler model fitting of i - E data and the steady-state photocurrent onset potential (Extended Data Fig. 4a vs. d). However, it has also been observed that the photocurrent onset potential of chopped-light photocurrent versus potential data is equal to the flat band potential determined in the dark, consistent with the model^{33,34}. Therefore, the chopped-light photocurrent onset potential may or may not differ from the flat band potential.

As the flat band potential is traditionally measured by capacitance measurements under dark conditions²⁴, and the photocurrent onset potential must be measured under illumination, we replace the term E_{fb} in Eq. S12 with the term $E_{\text{on,GB}}$, which represents the photocurrent onset potential predicted by the Gärtner-Butler model.

$$i = \eta qI_0\alpha\left(\frac{s}{S}\right)W = \eta qI_0\alpha\left(\frac{s}{S}\right)\sqrt{\frac{2\varepsilon\varepsilon_0(E-E_{\text{on,GB}})}{qN_d}} \quad \text{Eq. S13}$$

Eq. S13 predicts that the measured i onsets at $E_{\text{on,GB}}$ and that the measured i is proportional to $(E)^{1/2}$ and I_0 , which is what we observed for $E \geq -0.3$ V for bare and OEC-modified nanorods (see Extended Data Fig. 4a,c and Extended Data Fig. 8b-d). We defined this potential regime as being adequately described by the Gärtner model for quantitative analysis of the lock-in detected i - E data. Eq. S13 is presented as Eq. 1 in the Methods section in the main text.

3.6. Estimating N_d for these TiO₂ nanorods.

There is precedent in the literature that almost all of the elements detected by ICP-AES in Extended Data Fig. 6a can contribute to the observed n -type conductivity of these TiO₂ nanorods³⁵⁻⁴³. To estimate an N_d value, we first calculated N_d of the P25 nanoparticle and nanorod samples by assuming that all impurity atoms detected by ICP-AES (Extended Data Fig. 6a) were homogeneously distributed throughout the sample and every impurity atom acted as an electron donor to the lattice, giving rise to the observed n -type conductivity. The sum of all

atomic impurities relative to Ti for the nanoparticles (0.67%) and nanorods (6.87%) yielded N_d values of $2 \times 10^{20} \text{ cm}^{-3}$ and $2 \times 10^{21} \text{ cm}^{-3}$, respectively (bulk rutile has a density of $3.2 \times 10^{22} \text{ Ti atoms cm}^{-3}$). These estimated doping densities are orders of magnitude higher than the reported doping densities of P25 nanoparticle films (1×10^{17} to $5 \times 10^{17} \text{ cm}^{-3}$) determined via Mott-Schottky analysis^{44,45}.

Since this assumption leads to a gross overestimation of the P25 doping density, we then calculated a lower bound for N_d based on i - E data and compared it to the relative impurity concentrations of P25 and nanorod samples. Our ensemble i - E data (Extended Data Fig. 4a,c and Extended Data Fig. 8b,c) and nanorod-averaged single-nanorod i - E data (Extended Data Fig. 8d) is predicted by the Gartner model; i increases because the depletion layer thickness (W) concomitantly increases with $(E)^{1/2}$ according to Eq. S13. Our data indicates that W is not greater than the thickness of the nanorod. Therefore, we calculated a critical N_d value of $1.3 \times 10^{18} \text{ cm}^{-3}$ from Eq. S5 such that W is not larger than 86 nm (thinnest nanorod in the study) at $E - E_{\text{on,GB}} = 0.9 \text{ V}$ (determined from ensemble $E_{\text{on,GB}} = -0.66 \text{ V}$, see Extended Data Fig. 8d). This critical N_d value represents a lower bound on the doping density of the nanorod sample so that W is not larger than the thickness of any nanorod at $+0.2 \text{ V}$. This critical N_d value is an order of magnitude larger than the reported doping densities of P25 films. The order of magnitude increase in N_d of the nanorod sample compared to P25 is consistent with the data in Extended Data Fig. 6a, which shows that the total atomic impurity content relative to Ti is an order of magnitude higher in the nanorod sample than the P25 starting material. We thus estimated the doping density of the sample as 10^{18} cm^{-3} . It is notable that $N_d = 5 \times 10^{18} \text{ cm}^{-3}$ for undoped rutile TiO_2 nanorods synthesized via hydrothermal methods has been reported⁴⁶.

It should be noted that we fit single nanorod i - E data using Eq. S13 by only assuming that the nanorods are not fully depleted (e.g., W is not larger than the thickness of the nanorod). We fit the observed i - E data with Eq. S13 to obtain $\eta / N_d^{1/2}$ and $E_{\text{on,GB}}$, and by assuming an N_d value of 10^{18} cm^{-3} , we obtain η and $E_{\text{on,GB}}$. Assuming an N_d value allows one to obtain a physically meaningful η value for each nanorod spot. The particular value of N_d assumed has no effect on the relative distribution of η and the correlation of η with all other parameters.

4. Analysis of single-molecule rate data versus applied potential

4.1. Kinetic model for the photoelectrocatalytic oxidation of AR.

In our single-molecule fluorescence imaging experiments of photoelectrocatalytic oxidation of AR, the concentration of AR is low (e.g., 50 nM). The overall steady-state AR oxidation rate for ~ 1000 nanorods at $+0.2 \text{ V}$ is about 326 s^{-1} , calculated from the nanorod-averaged rate ($\sim 2 \times 10^{-5} \text{ molecules s}^{-1} \text{ nm}^{-2}$; Extended Data Fig. 3b) multiplied by the average structural properties of the nanorods ($62 \text{ nm} \times 263 \text{ nm} \approx 16,300 \text{ nm}^2$ in Supplementary Figure 1). This corresponds to 652 holes s^{-1} as AR oxidation is overall a two-hole oxidation reaction (Extended Data Fig. 1a). On the other hand, the overall photocurrent from these ~ 1000 nanorods on the ITO electrode at $+0.2 \text{ V}$ under the same 375 nm TIRF illumination geometry is about 20 nA (Extended Data Fig. 4d), corresponding to $\sim 10^{11} \text{ holes s}^{-1}$, which is about 9 orders of magnitude larger than the rate of AR oxidation. Thus AR oxidation contributes an insignificant fraction of all photoelectrocatalytic oxidations on the surface of TiO_2 nanorods, and water oxidation is the dominant reaction. Therefore, the AR molecules can be treated as a probe molecule that samples the steady-state surface concentration of photogenerated oxidative species, either the photogenerated h^+ or species like surface adsorbed OH^{\bullet} radical (we will show below that OH^{\bullet} radical is the direct oxidant of AR molecules). We can then write a general equation for the observed rate of AR oxidation:

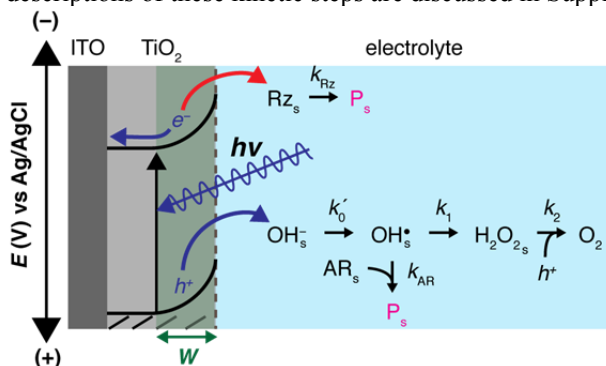
$$v_{\text{AR}} (\text{s}^{-1} \text{ nm}^{-2}) = k_{\text{AR}} [\text{AR}_s] [\text{ox}_s] \quad \text{Eq. S14}$$

where k_{AR} is a rate constant for AR oxidation, $[\text{AR}_s]$ is the surface concentration of AR, which depends on the AR concentration in the surrounding electrolyte solution, and $[\text{ox}_s]$ is the surface concentration of the oxidizing species that reacts with AR.

In the following, we describe a kinetic model for photoelectrooxidation of water on TiO_2 surfaces (schematically shown in Supplementary Scheme 4), which gives the expression for $[\text{ox}_s]$, so that we could model v_{AR} measured experimentally. This model includes a limited number of major irreversible reaction steps for water oxidation toward O_2 on a TiO_2 nanorod under anodic bias (listed in Supplementary Table 1), and the reactions

largely follow those by Salvador and co-workers^{33,47} and by Nozik and co-workers⁴⁸ for quantifying the rate of photoelectrocatalytic oxidation of organic molecules by TiO₂ in aqueous electrolyte. In this model, water oxidation by photogenerated holes is approximated to start with the oxidation of surface adsorbed water molecules or hydroxide to generate surface adsorbed hydroxyl radical (reactions 2a or 2b). The surface adsorbed hydroxyl radicals can combine to form hydrogen peroxide (reaction 3), which can be further oxidized by holes to generate O₂ (reaction 4). It is assumed³³ that the potential is sufficiently positive of $E_{\text{on,GB}}$ (more positive than -0.4 V as discussed in Section 0) so that all recombination reactions between electrons and holes, as well as electrons and photogenerated intermediates (e.g., OH[•] and H₂O₂), are sufficiently slow to be negligible kinetically, similarly to what was assumed by Salvador^{33,47}. Moreover, as the AR oxidation is only a tiny fraction of all possible oxidative reactions on the TiO₂ surface as described earlier, its contribution to the overall kinetics of water oxidation is not included.

Supplementary Scheme 4 | Detailed kinetic map that outlines the most important kinetic pathways for photogenerated holes and electrons. The detailed descriptions of these kinetic steps are discussed in Supplementary Table 1.



Supplementary Table 1. Major kinetic reactions included in the model for water oxidation on photo-excited TiO₂ nanorods^{33,48}

Charge carrier generation and hole flux to the surface	
<p><u>Reaction 1</u></p> $h_b^+ \xrightarrow{v_0^{h^+}} h_s^+$	$v_0^{h^+} = \frac{d[h_s^+]}{dt} = \frac{1}{A} \left(\frac{I_0}{S} s \right) \alpha \sqrt{\frac{2\epsilon\epsilon_0}{qN_d}} \sqrt{E - E_{on,GB}}$ <p>$v_0^{h^+}$ represents the hole flux to the surface ($s^{-1} \text{ cm}^{-2}$). h_b^+ is the hole in the bulk; h_s^+ is the hole transported to the surface. Charge carrier generation follows the Beer-Lambert absorption profile and separation of carriers follows the Gärtner model, where $\eta_{sep} = 1$. A represents the total electrochemically active surface area of the nanorod (does not include bottom face of the nanorod in contact with ITO). S is the laser beam illumination area. s is the nanorod geometric cross section perpendicular to the illumination laser. Other parameters are defined earlier in Section 3.3.</p>
Surface reactions	Rate law
<p><u>Reaction 2a</u></p> $\text{OH}_s^- + h_s^+ \xrightarrow{v_0'} \text{OH}_s^{\cdot}$ <p><u>Reaction 2b</u></p> $\text{H}_2\text{O}_s + h_s^+ \xrightarrow{v_0'} \text{OH}_s^{\cdot} + \text{H}^+$	<p><u>Reaction 2a</u></p> $v_0' = \frac{d[\text{OH}_s^{\cdot}]}{dt} = k_0' [h_s^+] [\text{OH}_s^-]$ <p><u>Reaction 2b</u></p> $v_0' = \frac{d[\text{OH}_s^{\cdot}]}{dt} = k_0' [h_s^+] [\text{H}_2\text{O}_s]$ <p>Here we do not differentiate the oxidation rates of surface adsorbed hydroxide and water. It is notable, however, that the point of zero zeta potential is 5.8⁴⁹ (the pH at which the net surface charge is zero), and therefore the TiO₂ surface at pH 8 is overall negatively charged, suggesting the surface is likely covered more with OH_s⁻ than H₂O. Nonetheless, we combine the above two equations as:</p> $v_0' = \frac{d[\text{OH}_s^{\cdot}]}{dt} = k_0' [h_s^+] [\text{OH}_s^- \text{ or } \text{H}_2\text{O}_s]$
<p><u>Reaction 3</u></p> $\text{OH}_s^{\cdot} + \text{OH}_s^{\cdot} \xrightarrow{v_1} \text{H}_2\text{O}_{2s}$	$v_1 = \frac{d[\text{H}_2\text{O}_{2s}]}{dt} = k_1 [\text{OH}_s^{\cdot}]^2$
<p><u>Reaction 4</u></p> $\text{H}_2\text{O}_{2s} + 2h_s^+ \xrightarrow{v_2} \text{O}_2 + 2\text{H}^+$	$v_2 = \frac{d[\text{O}_2]}{dt} = k_2 [h_s^+] [\text{H}_2\text{O}_{2s}]$ <p>Note this reaction consumes in total two h^+, but we assume that they are sequential reactions, as 3-body reactions are microscopically unlikely, and assume that the first hole oxidation step is rate limiting, so that the formation rate of O₂ is first order with respect to holes.</p>

We apply the steady state approximation to the intermediates $[h_s^+]$, $[\text{OH}_s^{\cdot}]$, $[\text{H}_2\text{O}_{2s}]$:

$$\begin{aligned} \frac{d[h_s^+]}{dt} = 0 &= \frac{1}{A} \left(\frac{I_0}{S} s \right) \alpha \sqrt{\frac{2\epsilon\epsilon_0}{qN_d}} \sqrt{E - E_{\text{on,GB}}} - k_0' [h_s^+] [\text{OH}_s^- \text{ or } \text{H}_2\text{O}_s] \\ &\quad - 2k_2 [h_s^+] [\text{H}_2\text{O}_{2s}] \\ &= \beta I_0 \sqrt{E - E_{\text{on,GB}}} - k_0' [h_s^+] [\text{OH}_s^- \text{ or } \text{H}_2\text{O}_s] - 2k_2 [h_s^+] [\text{H}_2\text{O}_{2s}] \end{aligned} \quad \text{Eq. S15}$$

$$\text{where } \beta = \left(\frac{s}{S} \right) \frac{\alpha}{A} \sqrt{\frac{2\epsilon\epsilon_0}{qN_d}}$$

$$\frac{d[\text{OH}_s^-]}{dt} = 0 = k_0' [h_s^+] [\text{OH}_s^- \text{ or } \text{H}_2\text{O}_s] - 2k_1 [\text{OH}_s^-]^2 \quad \text{Eq. S16}$$

$$\frac{d[\text{H}_2\text{O}_{2s}]}{dt} = 0 = k_1 [\text{OH}_s^-]^2 - k_2 [h_s^+] [\text{H}_2\text{O}_{2s}] \quad \text{Eq. S17}$$

We further made the following approximations to simplify the treatment:

1) The rate constants for hole capture by surface hydroxide or water k_0' is similar in magnitude to hole capture by hydrogen peroxide k_2 , e.g., $k_0' = k_2$, as approximated also by Salvador³³.

2) Due to the large excess of bulk hydroxide or water molecules, the surface concentration of the intermediate species $[\text{OH}_s^-]$ and $[\text{H}_2\text{O}_{2s}]$ are both significantly less than surface adsorbed hydroxide or water (i.e., $[\text{OH}_s^-]$ or $[\text{H}_2\text{O}_s]$). This is supported by the fact that the maximum theoretical surface coverage of hydroxide is $(5 \text{ to } 15) \times 10^{14} \text{ OH}^- \text{ cm}^{-2}$, depending on the specific crystal face of $\text{TiO}_2^{50,51}$, and Salvador used experimentally measured parameters from a bulk rutile crystal polarized at +0.6 V versus the flat band potential to calculate steady state $[\text{OH}_s^-]$ and $[\text{H}_2\text{O}_{2s}]$ concentrations to be only $8 \times 10^{12} \text{ cm}^{-2}$ and $8 \times 10^{13} \text{ cm}^{-2}$, respectively³³.

Using the above two approximations and solving Eq. S16, we yield the steady-state surface hole concentration $[h_s^+]$:

$$\begin{aligned} [h_s^+] &= \frac{\beta I_0 \sqrt{E - E_{\text{on,GB}}}}{k_0' [\text{OH}_s^- \text{ or } \text{H}_2\text{O}_s] + 2k_2 [\text{H}_2\text{O}_{2s}]} = \frac{\beta I_0 \sqrt{E - E_{\text{on,GB}}}}{k_0' ([\text{OH}_s^- \text{ or } \text{H}_2\text{O}_s] + 2[\text{H}_2\text{O}_{2s}])} \\ &= \frac{\beta I_0 \sqrt{E - E_{\text{on,GB}}}}{k_0' [\text{OH}_s^- \text{ or } \text{H}_2\text{O}_s]} \end{aligned} \quad \text{Eq. S18}$$

Inserting Eq. S18 into Eq. S16 yields:

$$\begin{aligned} \frac{d[\text{OH}_s^-]}{dt} = 0 &= k_0' [h_s^+] [\text{OH}_s^- \text{ or } \text{H}_2\text{O}_s] - 2k_1 [\text{OH}_s^-]^2 \\ &= k_0' \frac{\beta I_0 \sqrt{E - E_{\text{on,GB}}}}{k_0' [\text{OH}_s^- \text{ or } \text{H}_2\text{O}_s]} [\text{OH}_s^- \text{ or } \text{H}_2\text{O}_s] - 2k_1 [\text{OH}_s^-]^2 \\ &= \beta I_0 \sqrt{E - E_{\text{on,GB}}} - 2k_1 [\text{OH}_s^-]^2 \end{aligned} \quad \text{Eq. S19}$$

Rearranging the above equation gives the steady-state surface hydroxyl radical concentration $[\text{OH}_s^-]$:

$$[\text{OH}_s^-] = \sqrt{\frac{\beta I_0 \sqrt{E - E_{\text{on,GB}}}}{2k_1}} \quad \text{Eq. S20}$$

According to Eq. S18 and Eq. S20, the steady state surface concentrations of $[h_s^+]$ and $[\text{OH}_s^-]$ exhibit distinctly different dependences on light intensity and potential; $[h_s^+]$ scales with I_0 and $(E)^{1/2}$, whereas $[\text{OH}_s^-]$

scales with $(I_0)^{1/2}$ and $(E)^{1/4}$. The experimentally observed photoelectrocatalytic AR oxidation rate increased proportionally to $(E)^{1/4}$ (Extended Data Fig. 3b inset) at fixed light intensity and $I_0^{1/2}$ at fixed potential (e.g., +0.2 V, Extended Data Fig. 3c). Thus we conclude that AR reacts with surface adsorbed hydroxyl radical directly rather than with the surface holes.

The general expression of Eq. S14 can then be written as $v_{\text{AR}} = k_{\text{AR}}[\text{OH}_s^\bullet][\text{AR}_s]$. Note AR oxidation to P is overall a 2-hole oxidation process. We assume that the 2-hole oxidation reaction occurs sequentially (because 3-body reactions have low probability), and the first 1-hole oxidation step is rate limiting, and thus the formation of P is first order with respect to $[\text{OH}_s^\bullet]$ and the net reaction consumes two OH_s^\bullet . We insert Eq. S20 into the general rate equation for AR oxidation (and replacing the β term) to yield:

$$v_{\text{AR}} (\text{s}^{-1}\text{nm}^{-2}) = k_{\text{AR}} [\text{AR}_s] [\text{OH}_s^\bullet] = k_h \sqrt{I_0} \frac{\alpha s}{A S} \sqrt[4]{\frac{2\epsilon\epsilon_0 (E - E_{\text{on,GB}})}{qN_d}} \quad \text{Eq. S21}$$

where $k_h = \frac{k_{\text{AR}} [\text{AR}_s]}{\sqrt{2k_1}}$, and k_{AR} , k_1 , and $E_{\text{on,GB}}$ are unknown parameters, and $[\text{AR}_s]$ is held constant in all experiments. This k_h is an effective rate constant reflecting the surface h^+ -induced activity via hydroxyl radicals and it is independent of light intensity and applied potential. As the above derivation assumes $\eta_{\text{sep}} = 1$ for the hole flux (Reaction 1 in Supplementary Table 1), which is not true for real systems, the k_h here also contains contribution of the actual charge separation efficiency.

The mechanistic model is also consistent with Alivisatos et al.^{52,53} and our previous study⁵⁴ that AR reacts with OH^\bullet . Previously work by Majima and coworkers⁵⁵ also reported that the photogenerated hydroxyl radicals are immobile on the surface of rutile TiO_2 , further supporting that the AR oxidation reaction probes local surface h^+ activity on rutile TiO_2 nanorods studied here. Eq. S21 is presented as Eq. 2 in the main text and was used to fit single-molecule AR reaction rate data versus potential (Fig. 11 in the main text).

Units of k_h . We re-write Eq. S21 with units:

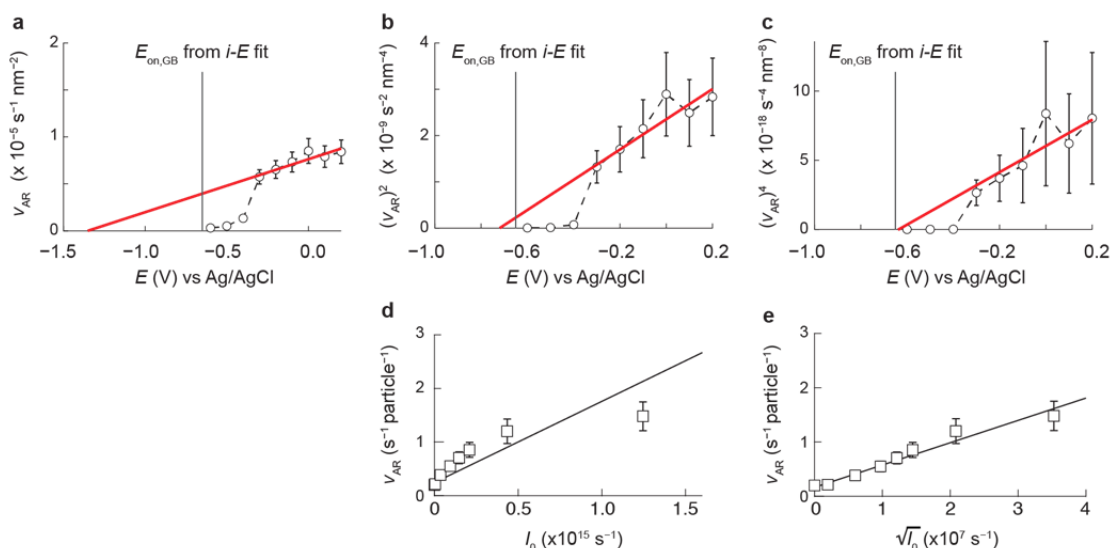
$$v_{\text{AR}} (\text{s}^{-1}\text{nm}^{-2}) = k_h \sqrt{I_0 (\text{s}^{-1})} \frac{\alpha (\text{cm}^{-1}) s (\text{cm}^2)}{A (\text{cm}^2) S (\text{cm}^2)} \sqrt[4]{\frac{2\epsilon\epsilon_0 (\text{C V}^{-1}\text{cm}^{-1}) [E - E_{\text{on,GB}} (\text{V})]}{q (\text{C}) N_d (\text{cm}^{-3})}} \quad \text{Eq. S22}$$

The experimental v_{AR} data was converted to units of $(\text{s}^{-1} \text{cm}^{-2})$, and the unit analysis of Eq. S22 can be simplified to:

$$\text{s}^{-1}\text{cm}^{-2} = k_h (\text{s}^{-1/2}\text{cm}^{-1}) \Rightarrow k_h = \text{s}^{-1/2} \text{cm}^{-1} \quad \text{Eq. S23}$$

Confirmation of the v_{AR} vs. $(E)^{1/4}$ and $I_0^{1/2}$ linear dependences. Supplementary Figure 12a-c compares the linear fit of v_{AR} , v_{AR}^2 , and v_{AR}^4 vs. E in the range of -0.3 to $+0.3$ V. The goodness of these three fits are comparable (between 0.88 and 0.92). However, they yield extremely different $E_{\text{on,GB}}$ where $v_{\text{AR}} = 0$. The $E_{\text{on,GB}}$ from linear $v_{\text{AR}}-E$ fitting is dramatically different from $E_{\text{on,GB}}$ determined from $i-E$ data analysis (Supplementary Figure 12a), thus ruling out the linear dependence of v_{AR} on E . The $E_{\text{on,GB}}$ from linear v_{AR}^2-E fit is also clearly more negative than that from $i-E$ analysis (Supplementary Figure 12a), which argues against, but does not rule out, the square-root dependence of v_{AR} on E . The $E_{\text{on,GB}}$ from linear v_{AR}^4-E fit reproduces that from $i-E$ analysis (Supplementary Figure 12c), supporting the $(E)^{1/4}$ scaling of v_{AR} .

Moreover, the mechanistic model predicts distinct v_{AR} dependences on potential and light intensity for OH^\bullet or direct hole AR oxidation pathways. We did not observe a $v_{\text{AR}}-(I_0)$ scaling relation (Supplementary Figure 12d), but clearly observed the $v_{\text{AR}}-(I_0)^{1/2}$ scaling beyond errors (Supplementary Figure 12e). Altogether, our data show that v_{AR} scales with $(E)^{1/4}$ and $(I_0)^{1/2}$, thus we conclude that AR reacts directly with surface adsorbed hydroxyl radical rather than with surface holes.



Supplementary Figure 12. Linear fitting (red lines) to (a) v_{AR} - E , (b) v_{AR}^2 - E , and (c) v_{AR}^4 - E data in the range of $E \geq -0.3$ V (data from Extended Data Figure 3b). The intercepts with the x-axis corresponds to $E_{on,GB}$. The vertical grey bar represents the $E_{on,GB}$ value determined from i - E data fitting. (d-e) Linear fits to v_{AR} versus I_0 and $(I_0)^{1/2}$, respectively, data from Extended Data Figure 3c.

4.2. Kinetic model for the photoelectrocatalytic reduction of Rz.

A general expression for the reduction rate, expressed as a current density, of an acceptor at a semiconductor electrode is given by Lewis⁵⁶:

$$J = qk_{et}n_s[A] \quad \text{Eq. S24}$$

where k_{et} is the rate constant for electron transfer ($\text{cm}^4 \text{s}^{-1}$), n_s is the surface concentration of electrons (cm^{-3}), and $[A]$ is the bulk concentration of acceptor molecules (cm^{-3}) (i.e., for the case that the electron transfer occurs to acceptor molecules in solution). For the photoelectrocatalytic reduction of Rz we study here, $[A]$ would refer to the surface concentration of Rz, as the reactions are surface-based, and, consequently the k_{et} would have the units of ($\text{cm}^3 \text{s}^{-1}$).

Reichman derived a model to describe the majority carrier (i.e., electrons for n -type semiconductors) collection efficiency at semiconductor-liquid junctions by solving the continuity equation of electrons in the depletion layer under illumination⁵⁷. The model predicts that, for photons absorbed close to the electrode/solution interface in semiconductors with low majority carrier mobility values, some excited majority carriers can diffuse to the interface against the electric field rather than being collected at the back contact. Given that the reported electron mobility ($\mu_n \approx 1 \times 10^{-4} \text{ cm}^2 \text{ V}^{-1} \text{ s}^{-1}$) of TiO_2 nanowires with similar dimensions to our nanorod sample⁵⁸ is approximately 4 orders of magnitude smaller than that for bulk rutile TiO_2 ⁵⁹, this effect is expected to be significant in our nanorods.

Reichman's general expression for the steady state majority carrier current density at the interface J_n is:

$$J_n = qv_c([e_{\text{light}}^- + e_{\text{dark}}^-]) \quad \text{Eq. S25}$$

where v_c is the majority carrier recombination velocity, $[e_{\text{light}}^-]$ is the excess electron concentration at the interface under illumination and $[e_{\text{dark}}^-]$ is the equilibrium electron concentration at the interface in the dark. The majority carrier recombination velocity v_c corresponds to the term $k_{et}[A]$ in Eq. S24 above and has units of cm s^{-1} ,⁵⁶ and it includes the contribution from all possible electron acceptors (i.e., v_c includes the rates of all reduction processes at the semiconductor-electrolyte interface).

For the TiO₂ nanorod system we studied, we experimentally observed that the rate of Rz reduction is only substantial under 375 nm laser illumination for the potentials applied in our study, and without UV light illumination, the observed Rz reduction is negligible (Extended Data Fig. 3e). Therefore, the dark contribution to the electron flux to the interface can be omitted for TiO₂ nanorods studied here. Reichman's expression for the steady state majority carrier current density at an illuminated *n*-type semiconductor-liquid junction is:

$$J_n = qv_c [e_{\text{light}}^-] = \frac{q\Phi_0}{\left(1 + \sqrt{\frac{2qN_d(E - E_{\text{on,GB}})}{\epsilon\epsilon_0}} \left[\frac{\mu_n}{v_c}\right]\right) \left(1 + \frac{1}{\alpha V_t} \sqrt{\frac{2qN_d(E - E_{\text{on,GB}})}{\epsilon\epsilon_0}}\right)} \quad \text{Eq. S26}$$

where $V_t = kT/q$, and μ_n is the electron mobility of rutile TiO₂ nanorods ($=10^{-4} \text{ cm}^2 \text{ V}^{-1} \text{ s}^{-1}$)⁵⁸, and $[e_{\text{light}}^-]$ is:

$$[e_{\text{light}}^-] = \frac{\Phi_0}{\left(v_c + \sqrt{\frac{2qN_d(E - E_{\text{on,GB}})}{\epsilon\epsilon_0}} \mu_n\right) \left(1 + \frac{1}{\alpha V_t} \sqrt{\frac{2qN_d(E - E_{\text{on,GB}})}{\epsilon\epsilon_0}}\right)} \quad \text{Eq. S27}$$

Modifying the light illumination term Φ_0 for our illumination geometry, e.g., replacing Φ_0 with $\left(\frac{I_0}{A}\right)\left(\frac{s}{S}\right)$, we have

$$[e_{\text{light}}^-] = \frac{\left(\frac{I_0}{A}\right)\left(\frac{s}{S}\right)}{\left(v_c + \sqrt{\frac{2qN_d(E - E_{\text{on,GB}})}{\epsilon\epsilon_0}} \mu_n\right) \left(1 + \frac{1}{\alpha V_t} \sqrt{\frac{2qN_d(E - E_{\text{on,GB}})}{\epsilon\epsilon_0}}\right)} \quad \text{Eq. S28}$$

Although Rz reduction to P is a total 2-electron reduction process, it is reasonable to assume that the 2-electron reduction reaction occurs sequentially, and the reduction rate is 1st-order with respect to the surface electron concentration. We can then write a general rate expression for Rz reduction in Eq. S29:

$$v_{\text{Rz}} = k_{\text{Rz}} [\text{Rz}_s] [e_{\text{light}}^-] \quad \text{Eq. S29}$$

where k_{Rz} ($\text{cm}^3 \text{ s}^{-1}$) is a rate constant and $[\text{Rz}_s]$ is the surface concentration of adsorbed Rz molecules (molecules cm^{-2}). Using Eq. S28 above, we have

$$v_{\text{Rz}} (\text{s}^{-1} \text{ nm}^{-2}) = k_e \frac{\left(\frac{I_0}{A}\right)\left(\frac{s}{S}\right)}{\left(v_c + \sqrt{\frac{2qN_d(E - E_{\text{on,GB}})}{\epsilon\epsilon_0}} \mu_n\right) \left(1 + \frac{1}{\alpha V_t} \sqrt{\frac{2qN_d(E - E_{\text{on,GB}})}{\epsilon\epsilon_0}}\right)} \quad \text{Eq. S30}$$

Here $k_e = k_{\text{Rz}} [\text{Rz}_s]$ and k_{Rz} , v_c , and $E_{\text{on,GB}}$ are unknown parameters; $[\text{Rz}_s]$ is a constant under our experimental conditions, as the solution concentration of Rz was kept constant. This k_e is an effective rate constant reflecting the surface e^- -induced activity and is independent of light intensity and applied potential. Eq. S30 is presented as Eq. 3 in the main text and was used to fit single-molecule Rz reaction rate data versus potential. As Reichman's model assumes every absorbed photon will produce an electron (majority carrier for *n*-type semiconductor) that can diffuse toward the surface, this k_e here also contains contribution of actual charge separation efficiency.

Units of k_e . After converting the experiment v_{Rz} data to units of ($\text{s}^{-1} \text{ cm}^{-2}$) and inserting units of $v_c = (\text{cm s}^{-1})$, $\mu_n = (\text{cm}^2 \text{ V}^{-1} \text{ s}^{-1})$ and $V_t = (\text{V})$, the units in Eq. S30 can be simplified to:

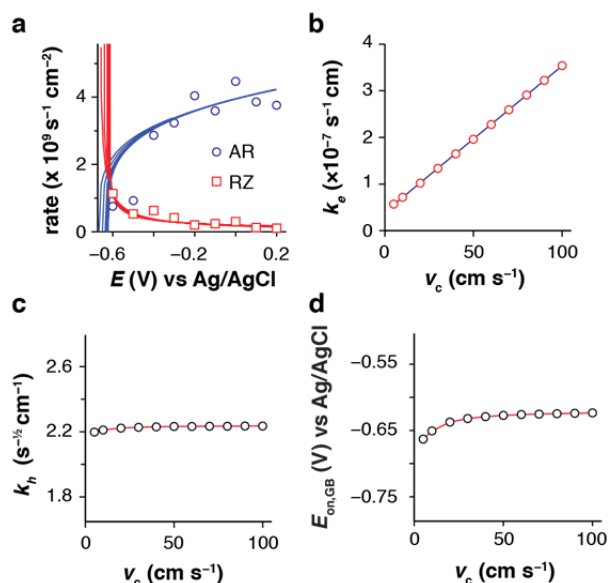
$$\text{s}^{-1} \text{ cm}^{-2} = k_e (\text{cm}^{-3}) \Rightarrow k_e = \text{cm s}^{-1} \quad \text{Eq. S31}$$

4.3. Procedures for fitting the potential dependences of AR oxidation and RZ reduction rates.

We used Eq. S21 and Eq. S30 to fit $v_{\text{AR}}-E$ and $v_{\text{RZ}}-E$ data, respectively. Both equations contain $E_{\text{on,GB}}$ as an unknown parameter. Since both measurements were performed in the same electrolyte and under the same light illumination conditions, we fit $v_{\text{AR}}-E$ for $E \geq -0.3$ V (see Section 0) and $v_{\text{RZ}}-E$ data for $E \geq -0.6$ V simultaneously while sharing the value of $E_{\text{on,GB}}$ and assuming $N_{\text{d}} = 10^{18} \text{ cm}^{-3}$ (see Section 3.6).

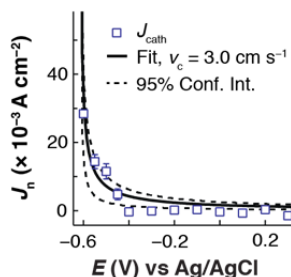
We were unable to decouple k_e from v_c by fitting $v_{\text{RZ}}-E$ data with Eq. S30. The former represents the fraction of photogenerated electrons that react with RZ whereas the latter represents the total consumption of photogenerated electrons at the interface. However, we found that k_e was linearly proportional to v_c with a well-defined slope (Supplementary Figure 13b), which was used to determine k_e by using a v_c value from ensemble measurements. Below we describe how we fit $v_{\text{AR}}-E$ and $v_{\text{RZ}}-E$ data sets simultaneously.

Determining k_e from the slope of k_e versus v_c . As mentioned above, we could not decouple k_e and v_c in fitting the $v_{\text{RZ}}-E$ data together with the $v_{\text{AR}}-E$ data on individual nanorod spots. To reduce the degree of freedom in data fitting, we assumed a value of v_c (e.g., over the range of 1 to 100 cm s^{-1} , see Section 4.4 below for determination of this range) while globally fitting the $v_{\text{AR}}-E$ and $v_{\text{RZ}}-E$ data with the $E_{\text{on,GB}}$ parameter shared. Supplementary Figure 13a shows representative fit results. We found that the fitted value of k_e shows a linear correlation with the value of v_c (Supplementary Figure 13b), where the slope varies from nanorod to nanorod and larger values indicate greater surface electron reactivity; in contrast, k_h and E_{fb} do not show much dependence on v_c , i.e., their values do not vary beyond $\pm 1.4\%$ and $\pm 4.1\%$ averaged over all nanorods, respectively, with v_c ranging from 1 to 100 cm s^{-1} (Supplementary Figure 13c and d). All of the results and conclusions in this study were identical if the slope was used to quantify the e^- reactivity of each nanorod spot. However, in order to provide a more physically meaningful reactivity parameter for each nanorod spot, rather than the aforementioned slope value, we determined the slope of k_e versus v_c and multiplied the slope by an experimentally-determined ensemble-averaged v_c (see Section 4.4) to yield k_e for each spot. For each nanorod spot, we determined the linear correlation between k_e and v_c , and the reported k_e value for each nanorod spot was determined by using this linear correlation multiplied by $v_c = 3.0 \text{ cm s}^{-1}$ (see Section 4.4 below). The reported $E_{\text{on,GB}}$ and k_h values are the averages of the results over the range of v_c assumed, such as in Supplementary Figure 13c-d, and the error bars are the standard deviations.



Supplementary Figure 13 | Representative global fit results of single-molecule $v_{\text{AR}}-E$ and $v_{\text{RZ}}-E$ data from a spot of a TiO₂ nanorod. **a**, Global fitting results when different values of v_c are assumed (blue and red lines) overlaid on $v_{\text{AR}}-E$ (blue circles) and $v_{\text{RZ}}-E$ (red squares) data. **b**, Fitted parameter k_e versus the input v_c . The solid blue line represents a linear fit (slope = $(3.13 \pm 0.01) \times 10^{-9}$) which was used to determine k_e at $v_c = 3.0 \text{ cm s}^{-1}$. **c-d**, The fitted k_h and E_{fb} versus input v_c , from which the average and standard deviation of all fitted k_h or $E_{\text{on,GB}}$ values were determined (average and standard deviation values for **c** was $2.23 \pm 0.01 \text{ s}^{-1/2} \text{ cm}^{-1}$ and **d** was $-0.63 \pm 0.01 \text{ V}$).

4.4. Determining an ensemble-averaged v_c from ensemble $i_{\text{cath}}-E$ data.



Supplementary Figure 14 | Estimation of v_c from the cathodic spike in the photocurrent transient data. An ensemble-averaged v_c value was determined from the ensemble $i_{\text{cath}}-E$ data (from photocurrent transient data in Extended Data Fig. 4b). We used the amplitude of the negative photocurrent spike immediately following interruption of the light pulse as a representative measurement of the steady-state majority carrier current because the cathodic spike represents the reaction between photogenerated conduction band electrons and all electron acceptors at the interface (e.g., h^+ , OH^+ , H_2O_2 , HO_2^+)^{33,60}. The cathodic photocurrent i_{cath} was divided by the estimated total geometric cross section of all TiO_2 particles in the illumination area to yield a cathodic photocurrent density J_n . The total geometric cross section of TiO_2 particles was estimated by thresholding SEM images and calculating the total coverage from 5 images. The fractional surface coverage of all TiO_2 particles on the ITO electrode surface was approximately 0.02. The power density of the 365 nm TIRF beam was used as Φ_0 . We fit $J_{\text{cath}}-E$ data (blue squares, represented as a positive value) with Eq. S26, Reichman's expression for steady-state majority carrier current at an n -type semiconductor-liquid junction, using $N_d = 10^{18} \text{ cm}^{-3}$ and $\mu_n = 1 \times 10^{-4} \text{ cm}^2 \text{ V}^{-1} \text{ s}^{-1}$ ⁵⁸ to obtain $v_c = 3.0 \pm 1.1 \text{ cm s}^{-1}$. The black line represents a fit to the data with Eq. S26, yielding an ensemble-averaged $v_c = 3.006 \text{ cm s}^{-1}$. We compared the magnitude of $v_c = 3.0 \text{ cm s}^{-1}$ obtained in to other v_c values obtained via the Reichman model. Lewis and co-workers previously reported a v_c value of 10^6 cm s^{-1} for amorphous hydrogenated Si in contact with Pd, whereas $v_c = 2 \times 10^3 \text{ cm s}^{-1}$ was obtained for the same electrode in contact with a liquid electrolyte, $\text{CH}_3\text{OH}-1.0 \text{ M LiClO}_4$, 0.1 mM dimethylferrocene⁺⁰ liquid junction⁶¹; semiconductor-liquid contacts exhibited lower v_c values than semiconductor-metal contacts. Although our value was three orders of magnitude smaller than the aforementioned value, we attribute the difference to the fact that v_c should depend on the concentration of electron acceptors⁵⁶ and we did not add external electron acceptors to the electrolyte; the electron acceptors here were photogenerated on the TiO_2 nanorod surface.

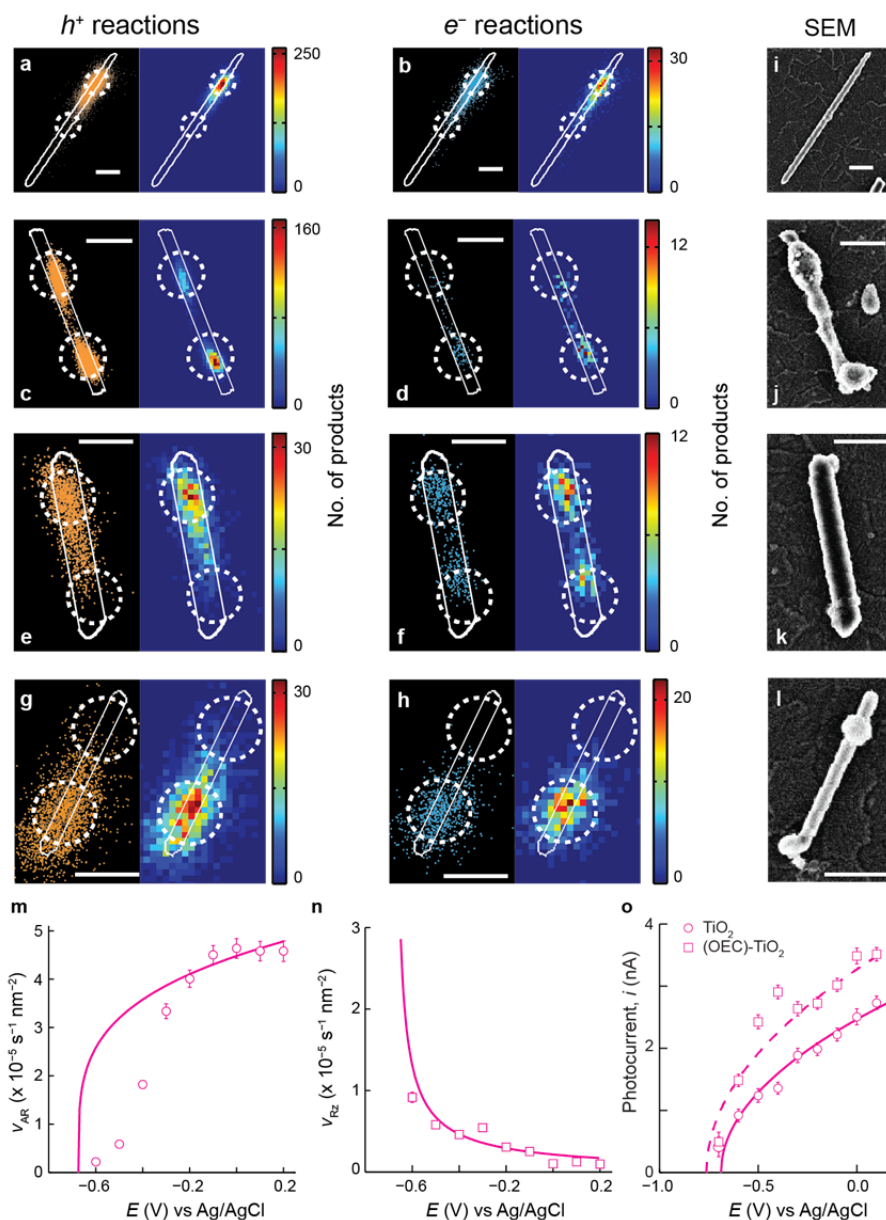
5. Additional Supplementary Data and Discussions

5.1. Quantitative super-resolution reaction imaging reveals reaction rate patterns and spatially correlated h^+ and e^- reactions.

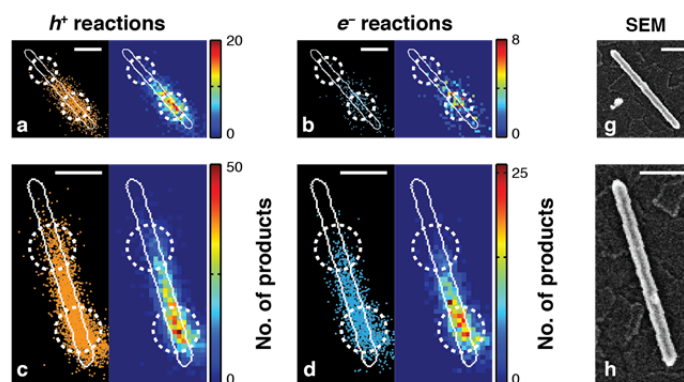
In this section, we present additional super-resolution reaction imaging data from single-nanorods, as well as nanorod-averaged results and more statistical analyses, that demonstrate localized (or delocalized) surface reactions and correlated h^+ and e^- activity (Supplementary Figure 15 to Supplementary Figure 17).

Moreover, our super-resolution reaction mapping showed that the *average* distance between the center of the hole hot-spot and the center of the corresponding electron hot-spot on the same nanorod is about $\sim 40 \text{ nm}$ (Extended Data Fig. 5d). This $\sim 40 \text{ nm}$ number is comparable to our localization precision and represents our resolution in co-localizing hole and electron activities. Within this $\sim 40 \text{ nm}$ colocalization resolution, there are two scenarios that we cannot *rigorously* differentiate: (1) the same types of active sites are responsible for both hole and electron activities, or (2) two different types of active sites mediate the respective hole and electron activities. However, we favor the former, because:

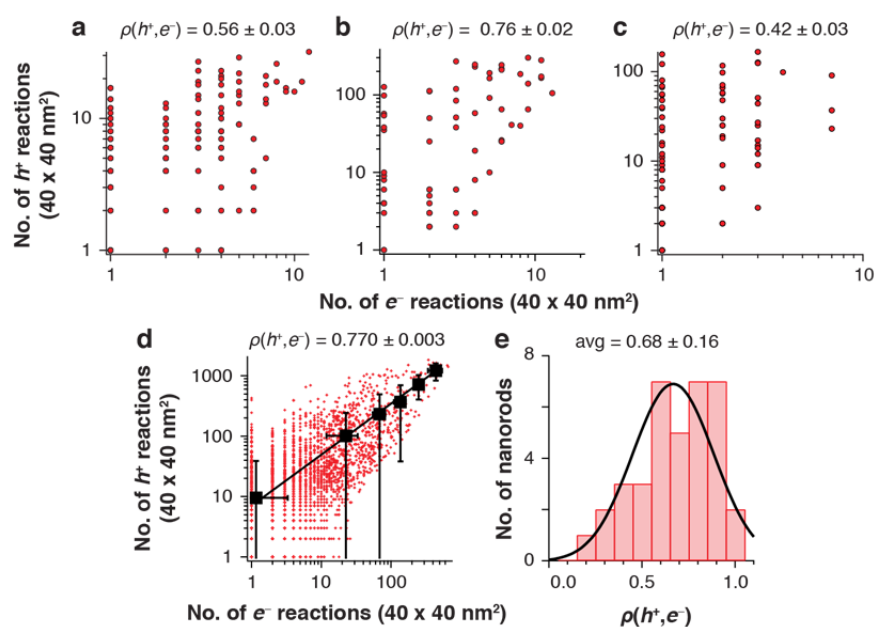
- Scenario 2 would require that the two different types of active sites responsible for respective hole and electron activities almost always co-localize within $\sim 40 \text{ nm}$, even during the high temperature molten-flux synthesis, which seems highly unlikely.
- Scenario 2 would also imply that we should be able to observe, at least occasionally, that the hot hole-spot does not co-localize with the hot electron-spot. But in fact, we never observe such behavior.



Supplementary Figure 15 | Additional quantitative super-resolution single-molecule reaction imaging reveals localized, correlated h^+ and e^- surface reactions. (a-l) The organization of the figure panels is identical to Figure 1 in the main text, except the data includes reactions probed by AR or Rz over the potential range -0.6 to $+0.2$ V. All scale bars = 400 nm. **m-o**, v_{AR} - E , v_{Rz} - E and i - E data for the nanorod “hot spot” shown in Fig. 1d-e of the main text.

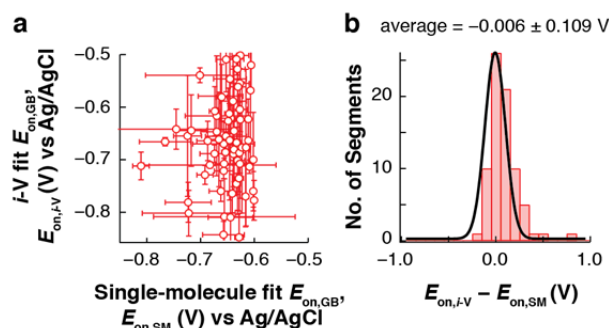


Supplementary Figure 16 | Quantitative super-resolution single-molecule reaction imaging reveals delocalized, correlated h^+ and e^- surface reactions. Same labeling scheme as Supplementary Figure 15, but for nanorods with delocalized reactions. All scale bars = 400 nm.



Supplementary Figure 17 | a-c, Quantitative correlation between h^+ and e^- surface reactions of single nanorods. Pixel to pixel correlation (black dots) between the two-dimensional histograms of h^+ and e^- surface reactions over the potential range of -0.6 to 0.2 V for the nanorod in Supplementary Figure 15e-f (a), Fig. 1d-e in the main text (c), and Supplementary Figure 15c-d (c). The calculated Pearson cross-correlation coefficient $\rho(h^+, e^-)$ for each rod is given in each figure. **d-e,** Nanorod-averaged correlation of h^+ and e^- reaction mapping. **d,** pixel to pixel correlation from the 2-D histograms of h^+ and e^- -electron induced reactions over the potential range of -0.6 to 0.2 V compiled from 37 nanorods. The data points were also grouped into 6 bins and averaged within each bin to obtain the general trend (black squares). Black line is a linear fit. Error bars are s.d. The overall cross correlation coefficient $\rho(h^+, e^-)$ is ~ 0.77 . **e,** histogram of correlation coefficients $\rho(h^+, e^-)$ calculated per nanorod as in (a-c) with an average value of 0.68.

5.2. There is no significant difference between $E_{\text{on,GB}}$ determined from i - E data and that from v_{AR} and v_{RZ} versus E data.



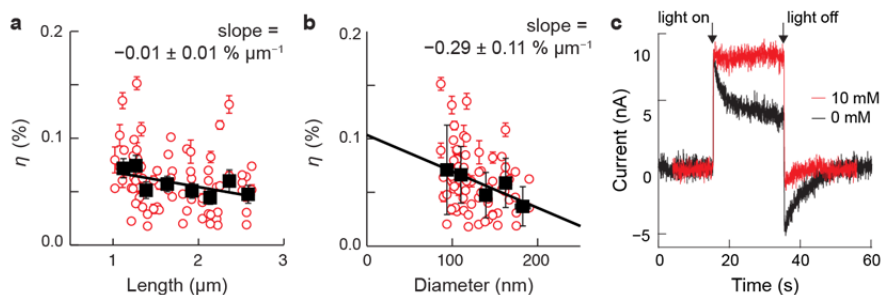
Supplementary Figure 18 | Single-molecule imaging and single nanorod photocurrent measurements were performed under different 375 nm light power density and with continuous and 1 Hz chopped illumination, respectively. Thus, we did not share the $E_{\text{on,GB}}$ parameter when fitting the i - E data and when fitting the v_{AR} and v_{Rz} vs. E data. **a**, Correlation plot between $E_{\text{on,GB}}$ determined from fitting i - E data and from global fitting of single-molecule v_{AR} and v_{Rz} vs. E data. Error bars represent s.d. The data points are scattered around the diagonal within error bars and there is essentially no correlation ($\rho = -0.12 \pm 0.08$) between the $E_{\text{on,GB}}$ values obtained from either method. **b**, Histogram of the difference in $E_{\text{on,GB}}$ values between the two analysis methods, where the black line is a Gaussian fit to the distribution. The average difference is around zero. We conclude that under our experimental conditions, and fitting the i - E data where the Gärtner model is applicable (i.e., $E \geq -0.3$ V) and globally fitting v_{AR} - and v_{Rz} - E data sets, there is no significant difference in $E_{\text{on,GB}}$ values within our experimental uncertainties.

5.3. The low average η value could be attributed to poor charge transport and inefficient charge transfer kinetics.

A general expression for the photocurrent at a semiconductor-liquid junction is $i = I_{\text{abs}} \times \eta_{\text{sep}} \times \eta_{\text{surf}}$, where I_{abs} refers to the number of absorbed photons (s^{-1}), η_{sep} is the efficiency of charge-carrier separation and transport to the collecting contacts and η_{surf} is the efficiency of charge transfer at the interface¹⁸. The absorbed photon to current efficiency within the depletion layer η determined via Eq. 1 in the main text contains contributions from η_{sep} and η_{surf} (SI Section 3), thus the low average value of η could be attributed to low η_{sep} and/or low η_{surf} .

Regarding contributions from η_{sep} to η , Supplementary Figure 19a shows that η has essentially no dependence on nanorod length, but Supplementary Figure 19b shows that η slightly decreases with increasing nanorod diameter. This decrease supports that charge transport in the nanorod plays a role in determining η , because for larger-diameter nanorods, the electrons have to travel longer distances to reach the ITO contact, during which the electrons would be scattered more by the impurities in the nanorod (Extended Data Fig. 6a)⁶². Therefore, the low η value could be attributed in part to poor charge transport in the nanorods.

Regarding contributions from η_{surf} to η , Fig. 2b in the main text shows that η is strongly correlated with k_h , an effective rate constant for surface hole reactions. Therefore, charge transfer kinetics at the interface plays a role in determining the magnitude of η , and the low η values could be attributed in part to inefficient charge transfer kinetics. To further demonstrate that charge transfer kinetics limits the water oxidation photocurrent efficiency of these TiO_2 nanorods, we followed the approach by Dotan et al¹⁸ and performed chopped light photocurrent measurements in the presence of a hole scavenger (i.e., acetate⁶³). The photocurrent transient decay upon light illumination is removed when 10 mM acetate is added to the aqueous electrolyte and the steady-state photocurrent is larger (Supplementary Figure 19c), indicating that acetate oxidation kinetics is faster than water oxidation kinetics on these nanorods. Thus, charge transfer kinetics limits the water oxidation photocurrent efficiency of these TiO_2 nanorods.

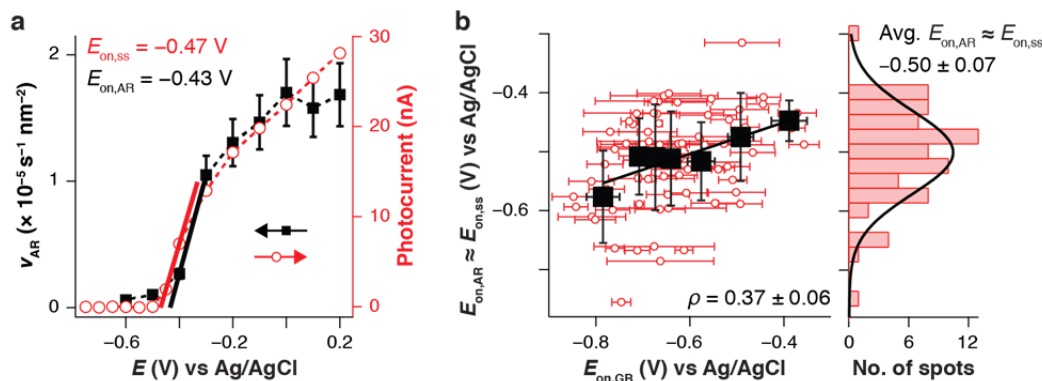


Supplementary Figure 19 | **a-b**, Dependence of η on nanorod length (**a**) and diameter (**b**). The red circles indicate data from 78 spots on 37 nanorods and the black squares represent averaged data after binning into groups of 10 data points by their lengths or diameters. The black lines in **a** and **b** are linear fits to the black squares. All error bars represent s.d. **η essentially has no dependence on nanorod length, while it decreases with increasing diameter.** **c**, Ensemble-level photocurrent versus time dynamics for TiO₂ nanorods at -0.35 V in the absence and presence of 10 mM sodium acetate.

We do not attribute variations in η to be caused mainly by variations in N_d because, according to Eq. S13, an order of magnitude increase in local N_d would decrease the photocurrent by merely a factor of 3 for $(E - E_{\text{on,GB}}) = 0.9$ V. Considering that the distribution of η spans almost an order of magnitude, a 2 orders of magnitude increase in local N_d would be required to account for the wide variation in η ; this magnitude of change in N_d seems less likely, even though variations of impurities are detected in STEM-EDX (Extended Data Fig. 6d-f).

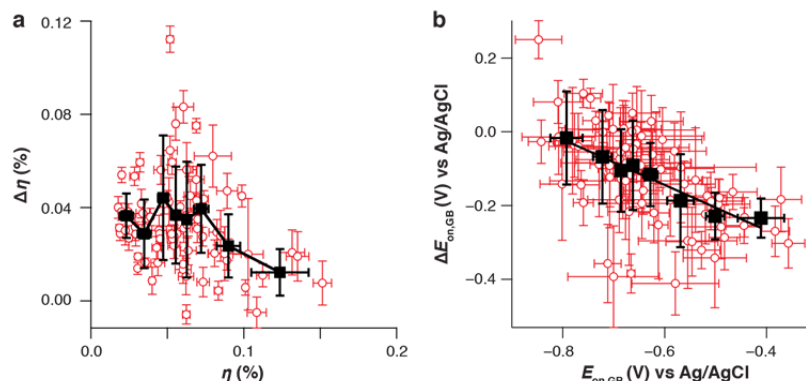
5.4. $E_{\text{on,GB}}$ is linearly correlated with $E_{\text{on,ss}}$, and thus values and changes of $E_{\text{on,GB}}$ reflect directly the values and changes of $E_{\text{on,ss}}$.

Here we show that for every nanorod spot, the fitted photocurrent onset potential $E_{\text{on,GB}}$ predicted by Eq. S13 is linearly correlated with its steady-state photocurrent onset potential $E_{\text{on,ss}}$.



Supplementary Figure 20 | **$E_{\text{on,GB}}$ is linearly correlated with $E_{\text{on,ss}}$.** **a**, Nanorod-averaged single-molecule AR oxidation rate versus potential (black squares) is compared with the ensemble measured steady-state photocurrent i_{ss} data (red circles) from Figure 1n in the main text. The steady state onset potentials for photocurrent ($E_{\text{on,ss}}$) and AR oxidation ($E_{\text{on,AR}}$) are defined as the intersection points of zero photocurrent or AR oxidation rate and the tangent at maximum slope of photocurrent or AR oxidation rate⁶⁴. Solid red and black lines indicate the linear fits to determine $E_{\text{on,ss}}$ and $E_{\text{on,AR}}$ respectively. **$E_{\text{on,AR}}$ is nearly the same as $E_{\text{on,ss}}$ within experimental error, and thus $E_{\text{on,AR}}$ is an effective indicator of $E_{\text{on,ss}}$.** **b**, Scatter plot of $E_{\text{on,AR}} (\approx E_{\text{on,ss}})$ versus $E_{\text{on,GB}}$ for 78 nanorod spots (red circles); a positive correlation was observed between the two values. The black squares represent averaged data in groups of 10, error bars represent s.d. The black line is a linear fit, clearly showing **that $E_{\text{on,GB}}$ is linearly correlated with $E_{\text{on,AR}}$ and thus $E_{\text{on,ss}}$. Therefore, the values and changes of $E_{\text{on,GB}}$ among individual nanorod spots are direct reflections of the values and changes of their $E_{\text{on,ss}}$.**

5.5. Co-B_i OEC deposition effects: 1) larger increase in η for nanorod spots with smaller initial η , and 2) larger negative shifts in $E_{\text{on,GB}}$ for nanorod spots with initially more positive $E_{\text{on,GB}}$.



Supplementary Figure 21 | **a**, The absolute change in η after Co-B_i catalyst deposition ($\Delta\eta = \eta_{\text{OEC}} - \eta$) versus the initial η showing that with increasing η , $\Delta\eta$ becomes smaller. Each data point (red circle) is from one nanorod spot. The black squares represent binned and averaged data in groups of 10 sorted by their η value. **b**, The absolute change in $E_{\text{on,GB}}$ ($\Delta E_{\text{on,GB}} = E_{\text{on,GB,OEC}} - E_{\text{on,GB}}$) after catalyst deposition versus the initial $E_{\text{on,GB}}$. The black squares represent binned and averaged data in groups of 10 sorted by $E_{\text{on,GB}}$. The solid lines are linear fits to the black squares to indicate the general trend. All error bars are S.D.

5.6. The large heterogeneity in η is likely *not* due to heterogeneity of contact resistances between individual nanorods and the ITO electrode.

The Gärtner-Butler model (Eq. S13) assumes that the applied potential E is entirely manifested as a potential drop across the depletion region of the semiconductor. It also assumes that the nanorod-ITO interface is an ohmic contact. However, significant contact resistance at the individual nanorod-ITO contact ($R_{\text{TiO}_2\text{-ITO}}$) could contribute to the overall series resistance (R_s) of the electrochemical cell. When R_s is significant, the applied potential appears across *both* the depletion region and R_s . In this section, we show that heterogeneous contact resistances between individual nanorods and the ITO electrode cannot account for the heterogeneity in η obtained from fitting the i - E data.

We simulated i - E curves using nanorod-averaged values of $\eta = 0.057\%$ and $E_{\text{on,GB}} = -0.66$ V as a function of R_s (red circles in Supplementary Figure 22a) according to El Guibaly et al⁶⁵, where the dependence of i on E in Eq. S13 is substituted by $(E - iR_s)$:

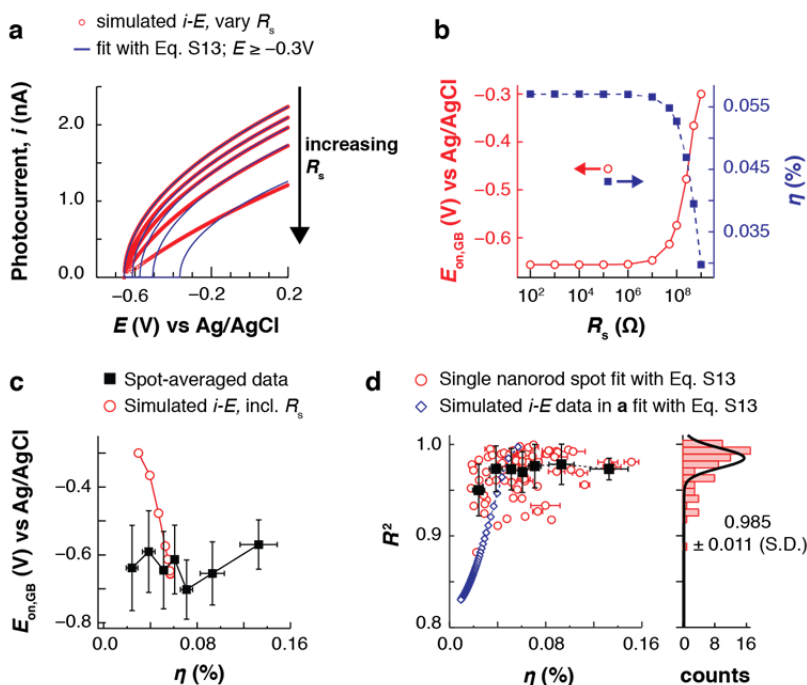
$$i = \eta q I_0 \alpha \left(\frac{s}{S} \right) \sqrt{\frac{2 \epsilon \epsilon_0 (E - iR_s - E_{\text{on,GB}})}{q N_d}} \quad \text{Eq. S32}$$

Qualitatively, with increasing R_s (from 0 to $10^9 \Omega$), the simulated i -vs.- E deviates more and more from the $(E)^{1/2}$ scaling relation; the saturating photocurrent at positive E decreases in magnitude.

We then fit each simulated i - E curve at different R_s with Eq. S13 for $E \geq -0.3$ V (blue lines, Supplementary Figure 22a), just as we treated the experimental data, and analyzed the fit parameters (η , E_{fb} , and the goodness of fit R^2 value) versus R_s . Supplementary Figure 22b shows that the fitted η and E_{fb} are independent of R_s over a large range of R_s from 0 to $10^6 \Omega$. These parameters only change significantly at very large R_s values ($> 10^6 \Omega$): η decreases and $E_{\text{on,GB}}$ shifts to more positive for $R_s > 10^6 \Omega$. The reason that the shifts in these parameters occur only at these very large R_s is that only nA photocurrent is passed in the cell. According to Frank and co-workers, reasonable values for $R_{\text{TiO}_2\text{-ITO}}$ are on the order of 1-10 Ω ⁶⁶, which is 6 orders of magnitude smaller than the values needed to decrease η by a factor of 2, as compared with the experimentally determined η from individual nanorod spots that can differ by a factor of ~ 7 (Supplementary Figure 22c).

Supplementary Figure 22c compares the correlation plot of $E_{\text{on,GB}}$ and η from fitting the simulated i - E curves at different R_s (red circles) and the experimentally determined $E_{\text{on,GB}}$ -vs.- η data from individual nanorod spots (black squares). The fitting results that include R_s contributions show that low η values (e.g., $< 0.08\%$) are associated with more positive $E_{\text{on,GB}}$. In contrast, there is no correlation between $E_{\text{on,GB}}$ and η in the experimental data (their cross correlation coefficients $\rho(\eta, E_{\text{on,GB}})$ from data in Figure 2c in the main text are -0.07 ± 0.08 and 0.15 ± 0.08 before and after OEC deposition, respectively).

The simulated i - E data in Supplementary Figure 22a also clearly show that R_s affects the scaling of i vs. $(E)^{1/2}$. The larger the R_s , the more i deviates from the $(E)^{1/2}$ scaling relation. Therefore, with increasing R_s , the fitting quality using the unmodified Eq. S13 decreases and the goodness of the fit R^2 for the simulated i - E curves at different R_s is strongly dependent on the fitted η (blue diamonds in Supplementary Figure 22d). In contrast, the R^2 from the experimental data is essentially independent of η (red circles in Supplementary Figure 22d). Taking all of the above results together, we conclude that the large heterogeneity in η is likely not due to heterogeneity of contact resistances between individual nanorods and the ITO electrode.



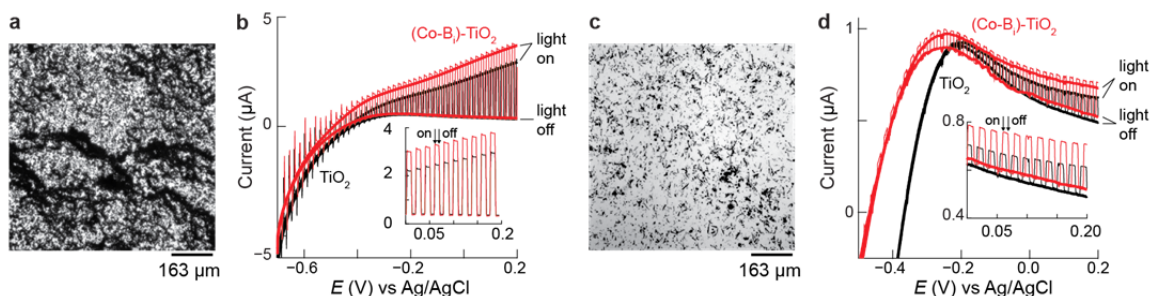
Supplementary Figure 22 | Effect of series resistance on i - E data fitting with Eq. S13. a, Simulated i - E curves (red circles) as a function of series resistance (R_s) using Eq. S32 and the nanorod-averaged $\eta = 0.057\%$ and $E_{\text{fb}} = -0.66$ V. The five curves are for $R_s = 0, 10^8, 2.5 \times 10^8, 5 \times 10^8,$ and $10^9 \Omega$, respectively. We then fit these simulated i - E curves at different R_s using Eq. S13 for $E \geq -0.3$ V (blue lines). b, Plot of $E_{\text{on,GB}}$ (red circles) and η (blue squares) versus R_s obtained from fitting the simulated i - E data in (a). c, Plot of $E_{\text{on,GB}}$ versus η from the fit results in (b) compared with experimental nanorod-averaged data from individual nanorod spots (black squares) from Extended Data Fig. 8d. d, Plot of R^2 values obtained from fitting the experimental data of individual nanorod spots with Eq. S13 versus η (red circles). The data was averaged in groups of 10 spots to show the general trend (black squares). The error bars represent s.d. The blue diamonds represent R^2 versus η obtained from fitting calculated i - E curves at different R_s . The right side of (d): the distribution of experimental R^2 values, and the black line is a Gaussian fit to the distribution with an average $R^2 = 0.985 \pm 0.011$ (s.d.).

5.7. The OEC-derived photocurrent enhancement reliably reflects an enhancement in water oxidation rates, and is not due to larger photocurrent transient dynamics that might complicate our lock-in detected chopped-light measurements.

To show that Co-B_i-enhanced photocurrent is not just due to photocurrent transient dynamics, we performed the chopped light ensemble-level experiments for a thick TiO₂ nanorod film sample (Supplementary

Figure 23a) prepared by drop-casting and for a predominantly single layer of TiO₂ nanorods sample (Supplementary Figure 23c) prepared by spin-coating. Supplementary Figure 23b and d overlay the linear sweep voltammograms (LSVs) under dark and continuous illumination conditions for the same two electrodes before and after OEC deposition (thick lines). The photocurrent (i.e., the current difference between light and dark conditions) of OEC-modified TiO₂ is significantly higher than that of bare TiO₂, demonstrating the OEC-caused photocurrent enhancement.

We further performed LSVs under 1 Hz chopped illumination (same frequency as used in single-nanorod photocurrent measurements; thin lines). For both samples, the photocurrent of OEC-modified TiO₂ is enhanced compared with the bare TiO₂. In the potential range of $E \geq -0.3$ V where we analyze the photocurrent with the Gartner-Butler model, the photocurrent transient behaviors are not discernible for the single-layer nanorod sample (Supplementary Figure 23d and inset). For the thick film sample, the photocurrent transient spikes are extremely small in amplitude (Supplementary Figure 23b and inset) and eventual steady-state current dominates the chopped photocurrent response (~94%). Therefore, the OEC-derived photocurrent enhancement from our lock-in detected chopped measurements is not due to a change in photocurrent transient dynamics, but reliably reflects an enhancement in water oxidation rates.

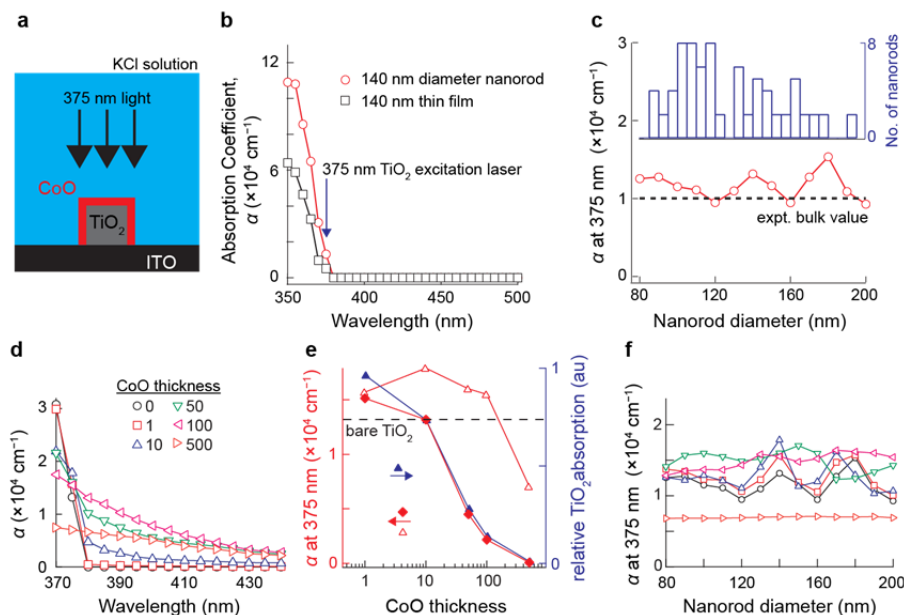


Supplementary Figure 23 | **a**, 10 \times optical transmission image of a thick nanorod film prepared by drop-casting. **b**, Linear sweep voltammograms of the sample in **a**. Black lines represent data from bare TiO₂ nanorods under 1 Hz chopped (thin lines) and continuous (thick lines) 13.3 mW/cm² 365 nm LED illumination in N₂-purged 1M KCl, 100 mM pH 8.3 borate buffer. Co-B_i catalyst was then photoelectrochemically deposited onto the same sample at 0.0 V at 13.3 mW/cm² until a saturated photocurrent enhancement was reached (~8 seconds) in 100 mM borate buffer containing 0.5 mM CoCl₂, and evaluated under the same chopped and continuous illumination conditions (red thin and thick lines). Dark scans are also shown for bare and Co-B_i samples as thick black and red lines, respectively. The inset shows minimal photocurrent transient dynamics over the more positive potential range. **c**, 10 \times optical transmission image of a predominantly single layer of TiO₂ nanorods prepared by spin-coating. **d**, LSV data for the sample in **c**, under same conditions as **b**, but the saturated photocurrent enhancement during catalyst deposition was achieved in 35 seconds. The inset shows negligible photocurrent transient dynamics.

5.8. Nano-optical antenna effects change the absolute magnitudes of η , k_h , and k_e , but do not affect their correlations and their trends from which we draw our scientific conclusions.

Finite-difference frequency-domain (FDFD) simulations were performed with COMSOL Multiphysics using the real and imaginary components of the refractive indices of rutile TiO₂ and ITO (taken from <https://www.filmetrics.com/refractive-index-database/>). The detailed computational methods are the same as those used to model light absorption by single Si nanowire PV devices in a similar illumination geometry as ours⁶⁷. Briefly, three-dimensional optical simulations were performed using the same illumination geometry as in our single-nanorod photocurrent measurements (Supplementary Figure 24a), where the laser beam illuminates the nanorod at normal incidence. The geometry is not chiral, nor does it have unusual anisotropies, so we simulated the circularly polarized laser beam by averaging the electric field being along the rod long axis or perpendicular to it). From these simulations we obtained the absorption coefficient α of the nanorod compared to a thin film of identical thickness (Supplementary Figure 24b). The nanorod's supra-band gap light absorption (<390 nm) is greater than its bulk counterpart due to nano-optical effects. At a fixed wavelength (e.g., 375 nm that was used to

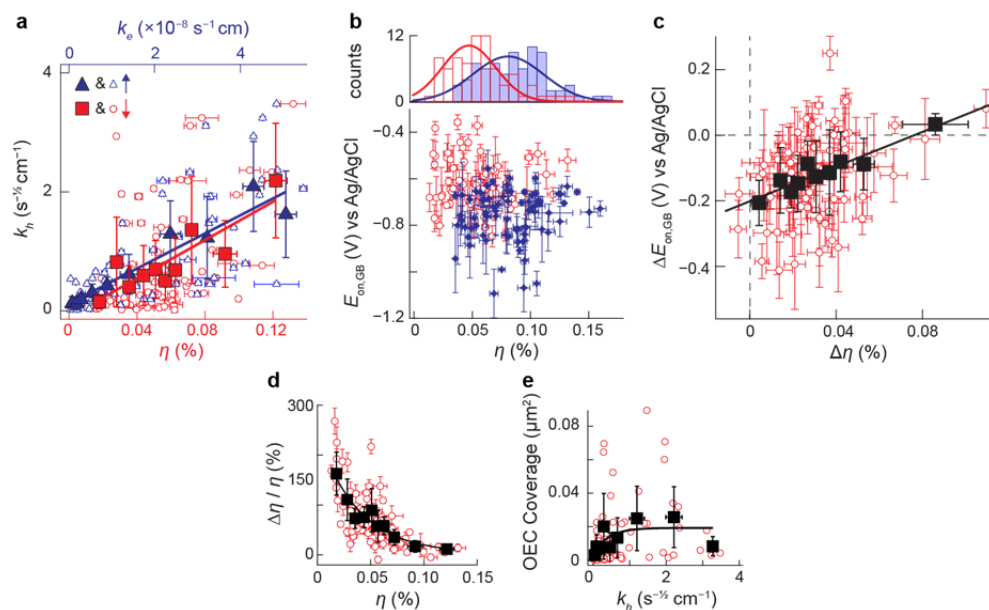
excite the TiO₂ nanorods), α further shows some dependence on the nanorod diameter (Supplementary Figure 24c). However, we will show below (Supplementary Figure 25) that using the FDTD-calculated α , which takes into account the nano-optical effect and the specific diameter of each nanorod, only slightly affects the absolute magnitudes of η , k_h and k_e , but it does not affect their correlations and their trends from which we draw our scientific conclusions.



Supplementary Figure 24 | Nano-optical effects in affecting the absorption coefficient of TiO₂ and cobalt-oxide-modified TiO₂ nanorods. **a**, Experimental geometry used for optical simulations. **b**, Calculated absorption coefficient α for a 140 nm thick rutile TiO₂ thin film and a 140 nm wide/thick and 1735 nm long nanorod, corresponding to the mean diameter and length of the nanorod sample, both on top of ITO substrates. **c**, Calculated absorption coefficient α at 375 nm versus nanorod diameter (red circles). The dashed line represents the experimental bulk $\alpha_{375 \text{ nm}}$ ²⁵, which we used in the manuscript. The diameter distribution of the nanorods we measured is overlaid for reference. **(d)** Calculated absorption coefficient α for the nanostructure in **a** for various catalyst thicknesses. **(e)** α at 375 nm of the nanostructure (left axis, open red triangles, data from **d**), the effective absorption coefficient by TiO₂ (i.e., $\alpha \times$ fraction of light absorbed by TiO₂, left axis, solid red diamonds) and relative TiO₂ light absorption (right axis, solid blue triangles) versus catalyst thickness. **(f)** Calculated absorption coefficient α at 375 nm versus nanorod diameter at different catalyst layer thickness; symbols coded as in **d**.

We used the diameter-dependent absorption coefficient values in Supplementary Figure 24c to recalculate η , k_h and k_e for every nanorod spot and re-plotted all main text figures that contain these parameters (Supplementary Figure 25). Importantly, all of the following trends hold:

- (1) Spots with larger η expectedly have larger k_h ($\rho(k_h, \eta) = 0.45 \pm 0.06$; Supplementary Figure 25a).
- (2) k_h of each spot is also strongly correlated with its k_e ($\rho(k_h, k_e) = 0.76 \pm 0.03$; Supplementary Figure 25a).
- (3) On average, η increases by $\sim 70\%$ following OEC deposition (Supplementary Figure 25b). The absolute values of η are now smaller because the corrected α is larger.
- (4) For those spots with $\Delta E_{\text{on,GB}} < 0$ V, the magnitude of $\Delta E_{\text{on,GB}}$ is smaller for spots with larger $\Delta\eta$, i.e., $\Delta E_{\text{on,GB}}$ and $\Delta\eta$ are anticorrelated (Supplementary Figure 25b). 16% of the spots still have positive $E_{\text{on,GB}}$ shifts.
- (5) A strong negative correlation exists for the relative change in η vs initial η (Supplementary Figure 25d).
- (6) More catalyst material is deposited onto higher activity sites (Supplementary Figure 25e).



Supplementary Figure 25. Recalculated k_h , k_e and η data using diameter-dependent absorption coefficients taking into account nano-optical effects on nanorod absorption coefficient. **a**, Correlation of k_h with η and with k_e ; ($\rho(k_h, \eta) = 0.45 \pm 0.06$) and ($\rho(k_h, k_e) = 0.76 \pm 0.03$). **b**, $E_{\text{on,GB}}$ vs. η before and after OEC deposition. Top: Distribution of η ; lines are Gaussian fits, giving for TiO_2 : $\eta = 0.048 \pm 0.023\%$, and for (OEC)- TiO_2 : $\eta_{\text{OEC}} = 0.082 \pm 0.030\%$. **c**, Correlation between $\Delta E_{\text{on,GB}}$ and $\Delta\eta$. **(d)** Relative change in η versus initial η . **(e)** Catalyst coverage vs. k_h .

To quantitatively evaluate the optical cross section of (Co-Bi)-based OECs, we performed FDFD simulations of a variable thickness cobalt oxide⁶⁸ layer on TiO_2 nanorods (Supplementary Figure 24a). The calculated absorption spectra of the nanostructure indicates that absorption at > 380 nm increases with increasing catalyst layer thickness (Supplementary Figure 24d), consistent with previous reports⁶⁹. However, at 375 nm which we used to excite the nanorods, the change in absorption coefficient is not monotonic: there is a ~ 17 -36% increase in α_{375} for catalyst thicknesses ranging from 1 - 100 nm, followed by a decrease when the cobalt-oxide thickness reaches ~ 500 nm (Supplementary Figure 24e, red open triangles). (The thickness of our deposited catalyst layer varies from < 10 to 400 nm, e.g., Fig. 1h-j and Supplementary Figure 15i, j, k, l). As the catalyst layer thickness increases, the fraction of the light that is absorbed by the underlying TiO_2 nanorod decreases monotonously (Supplementary Figure 24e, blue triangles), and the effective absorption coefficient by TiO_2 (i.e., $\alpha \times$ fraction of light absorbed by TiO_2) is at most 14% larger than that of bare TiO_2 for catalyst thicknesses of 1-10 nm and becomes significantly smaller than the bare TiO_2 for catalyst thicknesses > 10 nm (Supplementary Figure 24e, solid red diamonds). Finally, there are some diameter-dependent optical effects over a range of catalyst layer thicknesses (i.e., variation $\sim 30 \pm 20\%$; Supplementary Figure 24f).

Here we consider two scenarios regarding how the catalyst-induced changes in absorption may affect the photocurrent:

Scenario 1: The light absorption by the catalyst does not contribute to the photocurrent, which is consistent with reports that the catalyst does not contribute directly to photocurrent (Co-Pi on ZnO ⁷⁰; Co-Pi on Fe_2O_3 ⁶⁴). Under this scenario, the catalyst in the thickness range of up to 10 nm would increase the TiO_2 light absorption by maximally 14% (Supplementary Figure 24e, solid red diamonds). However, our measured relative photocurrent efficiency enhancement $\Delta\eta/\eta$ can be $\sim 200\%$ for low activity sites that have the least amount of catalyst deposited (Fig 3a, c in the main text). Therefore, an increase in light absorption by the OEC-modified TiO_2 can only account for a small fraction of the observed $\Delta\eta$. For catalyst thickness > 10 nm, which would be more relevant for higher activity sites that have more catalyst deposited, the OEC actually decreases the TiO_2 light absorption and therefore the observed $\Delta\eta$ must come from other catalyst effects (e.g., increased surface kinetics). Moreover, our data in Extended Data Fig. 9b shows that the observed photocurrent increase shows a saturation behavior with increasing OEC deposition time (thus OEC deposition amount), in contrast to the monotonous

decrease of the TiO₂ absorption with increasing OEC thickness (Supplementary Figure 24e, solid red diamonds), which further supports that the observed $\Delta\eta$ cannot be dominated by the OEC optical effect and must be affected by other factors (e.g., increased surface kinetics).

Scenario 2: The light absorption by the catalyst contributes equally to the photocurrent as that by the TiO₂ nanorod. Under this scenario, the catalyst in the thickness range of up to 100 nm would increase the OEC-TiO₂ nanorod by ~36% relative to the bare nanorod (Supplementary Figure 24e, open red triangles), which again cannot sufficiently account for the maximally ~200% (Fig 3a in the main text) and on average 60% increase (Fig. 2c, top, in the main text) of photocurrent efficiency. For catalyst thickness > 100 nm, the light absorption of OEC-TiO₂ is lower than the bare rod, and thus cannot account for the observed positive $\Delta\eta$.

Although the many contributions to the $\Delta\eta$ after catalyst deposition are not yet clearly defined and may include changes in the light absorption, the $\Delta\eta$, as defined in our model, is a direct reflection of the photocurrent enhancement caused by catalyst deposition. Above all, the anticorrelation of $\Delta\eta/\eta$ vs. η (and k_h and k_e) holds, which indicates that the optimal sites for photocurrent enhancement are the initially low efficiency and low activity sites.

In summary, our ensemble-level and nanorod-averaged photoelectrochemical measurements are consistent with literature that reported photocurrent increases and negative onset potential shifts for Co-based OEC-modified metal-oxide photoanodes. Regardless of the detailed nano-optical effects that may occur as a result of OEC deposition and whether or not the OEC-induced $\Delta\eta$ is mainly due to surface kinetics increase, our conclusion stays solid that the optimal catalyst deposition sites on these nanorods for photocurrent enhancement are the lower activity sites.

6. Additional references

- 1 Liu, B. *et al.* Large-scale synthesis of transition-metal-doped tio2 nanowires with controllable overpotential. *J. Am. Chem. Soc.* **135**, 9995-9998 (2013).
- 2 Giocondi, J., Salvador, P. & Rohrer, G. The origin of photochemical anisotropy in srtio3. *Top. Catal.* **44**, 529-533 (2007).
- 3 Tian, B., Kempa, T. J. & Lieber, C. M. Single nanowire photovoltaics. *Chem. Soc. Rev.* **38**, 16-24 (2009).
- 4 Tian, B. *et al.* Coaxial silicon nanowires as solar cells and nanoelectronic power sources. *Nature* **449**, 885-889 (2007).
- 5 Kelzenberg, M. D. *et al.* Photovoltaic measurements in single-nanowire silicon solar cells. *Nano Lett.* **8**, 710-714 (2008).
- 6 Liu, M., de Leon Snapp, N. & Park, H. Water photolysis with a cross-linked titanium dioxide nanowire anode. *Chem. Sci.* **2**, 80-87 (2011).
- 7 Hiesgen, R. & Meissner, D. Local nanoscale photocurrent characterization of semiconductor interfaces by scanning tunneling microscopy. *Electrochim. Acta* **42**, 2881-2888 (1997).
- 8 Furtak, T. E., Canfield, D. C. & Parkinson, B. A. Scanning light - spot analysis of the carrier collection in liquid - junction solar energy converters. *J. Appl. Phys.* **51**, 6018-6021 (1980).
- 9 Butler, M. A. Localized photoelectrochemical measurements of passive films on titanium. *J. Electrochem. Soc.* **130**, 2358-2362 (1983).
- 10 Kozlowski, M. R., Tyler, P. S., Smyrl, W. H. & Atanasoski, R. T. Photoelectrochemical microscopy of oxide films on metals: Ti/tio2 interface. *Surf. Sci.* **194**, 505-530 (1988).
- 11 Flaisher, H. & Tenne, R. Investigation into the photocurrent quadrature signal of photoelectrochemical cells. *J. Appl. Phys.* **56**, 2930-2938 (1984).
- 12 Chen, T.-Y. *et al.* Concentration and chromosome-organization dependent regulator unbinding from DNA for transcription regulation in living *escherichia coli* cells. *Nat. Commun.* **6**, 7445 (2015).
- 13 Thompson, R. E., Larson, D. R. & Webb, W. W. Precise nanometer localization analysis for individual fluorescent probes. *Biophys. J.* **82**, 2775-2783 (2002).

- 14 Yildiz, A. *et al.* Myosin v walks hand-over-hand: Single fluorophore imaging with 1.5-nm localization. *Science* **300**, 2061-2065 (2003).
- 15 Zhou, X. *et al.* Quantitative super-resolution imaging uncovers reactivity patterns on single nanocatalysts. *Nat. Nanotechnol.* **7**, 237-241 (2012).
- 16 Eells, W. C. Formulas for probable errors of coefficients of correlation. *J. Am. Stat. Assoc.* **24**, 170-173 (1929).
- 17 Xu, W. *et al.* Single-molecule electrocatalysis by single-walled carbon nanotubes. *Nano Lett.* **9**, 3968-3973 (2009).
- 18 Dotan, H., Sivula, K., Gratzel, M., Rothschild, A. & Warren, S. C. Probing the photoelectrochemical properties of hematite (α - Fe_2O_3) electrodes using hydrogen peroxide as a hole scavenger. *Energy Environ. Sci.* **4**, 958-964 (2011).
- 19 Gärtner, W. W. Depletion-layer photoeffects in semiconductors. *Phys. Rev.* **116**, 84-87 (1959).
- 20 Butler, M. A. Photoelectrolysis and physical properties of the semiconducting electrode WO_3 . *J. Appl. Phys.* **48**, 1914-1920 (1977).
- 21 Bard, A. J., Memming, R. & Miller, B. Terminology in semiconductor electrochemistry and photoelectrochemical energy conversion. *Pure Appl. Chem.* **63**, 569-596 (1991).
- 22 Gomes, W. P. & Cardon, F. Electron energy levels in semiconductor electrochemistry. *Prog. Surf. Sci.* **12**, 155-215 (1982).
- 23 Fàbrega, C. *et al.* Tuning the fermi level and the kinetics of surface states of TiO_2 nanorods by means of ammonia treatments. *J. Phys. Chem. C* **117**, 20517-20524 (2013).
- 24 De Gryse, R., Gomes, W. P., Cardon, F. & Vennik, J. On the interpretation of mott - schottky plots determined at semiconductor/electrolyte systems. *J. Electrochem. Soc.* **122**, 711-712 (1975).
- 25 Lindquist, S. E., Finnström, B. & Tegnér, L. Photoelectrochemical properties of polycrystalline TiO_2 thin film electrodes on quartz substrates. *J. Electrochem. Soc.* **130**, 351-358 (1983).
- 26 Hoang, S., Guo, S., Hahn, N. T., Bard, A. J. & Mullins, C. B. Visible light driven photoelectrochemical water oxidation on nitrogen-modified TiO_2 nanowires. *Nano Lett.* **12**, 26-32 (2011).
- 27 Salvador, P. Influence of pH on the potential dependence of the efficiency of water photo - oxidation at n - TiO_2 electrodes. *J. Electrochem. Soc.* **128**, 1895-1900 (1981).
- 28 Warren, S. C. *et al.* Identifying champion nanostructures for solar water-splitting. *Nat Mater* **12**, 842-849 (2013).
- 29 Bolts, J. M. & Wrighton, M. S. Correlation of photocurrent-voltage curves with flat-band potential for stable photoelectrodes for the photoelectrolysis of water. *J. Phys. Chem.* **80**, 2641-2645 (1976).
- 30 Wilson, R. H. A model for the current - voltage curve of photoexcited semiconductor electrodes. *J. Appl. Phys.* **48**, 4292-4297 (1977).
- 31 Cooper, G., Turner, J. A. & Nozik, A. J. Mott - schottky plots and flatband potentials for single crystal rutile electrodes. *J. Electrochem. Soc.* **129**, 1973-1977 (1982).
- 32 Tafalla, D., Pujadas, M. & Salvador, P. Direct measurements of flat-band potential shifts under illumination of the semiconductor-electrolyte interface by electrolyte electroreflectance. *Surf. Sci.* **215**, 190-200 (1989).
- 33 Salvador, P. Kinetic approach to the photocurrent transients in water photoelectrolysis at n-titanium dioxide electrodes. 1. Analysis of the ratio of the instantaneous to steady-state photocurrent. *J. Phys. Chem.* **89**, 3863-3869 (1985).
- 34 Sagara, T. & Sukigara, M. Photogenerated surface states at n - TiO_2 / aqueous solution interface. *J. Electrochem. Soc.* **135**, 363-367 (1988).
- 35 Choi, Y. J., Seeley, Z., Bandyopadhyay, A., Bose, S. & Akbar, S. A. Aluminum-doped TiO_2 nano-powders for gas sensors. *Sensors and Actuators B: Chemical* **124**, 111-117 (2007).
- 36 Mowbray, D. J., Martinez, J. I., Lastra, J. M. G., Thygesen, K. S. & Jacobsen, K. W. Stability and electronic properties of TiO_2 nanostructures with and without b and n doping. *J. Phys. Chem. C* **113**, 12301-12308 (2009).
- 37 Lu, N. *et al.* Fabrication of boron-doped TiO_2 nanotube array electrode and investigation of its photoelectrochemical capability. *J. Phys. Chem. C* **111**, 11836-11842 (2007).

- 38 Li, W. *et al.* Improve photovoltaic performance of titanium dioxide nanorods based dye-sensitized solar cells by ca-doping. *Mater. Res. Bull.* **57**, 177-183 (2014).
- 39 Roldán, A., Boronat, M., Corma, A. & Illas, F. Theoretical confirmation of the enhanced facility to increase oxygen vacancy concentration in TiO_2 by iron doping. *J. Phys. Chem. C* **114**, 6511-6517 (2010).
- 40 Alivov, Y., Singh, V., Ding, Y., Cerkovnik, L. J. & Nagpal, P. Doping of wide-bandgap titanium-dioxide nanotubes: Optical, electronic and magnetic properties. *Nanoscale* **6**, 10839-10849 (2014).
- 41 Liu, Q. Photovoltaic performance improvement of dye-sensitized solar cells based on mg-doped TiO_2 thin films. *Electrochim. Acta* **129**, 459-462 (2014).
- 42 Huang, F., Li, Q., Thorogood, G. J., Cheng, Y.-B. & Caruso, R. A. Zn-doped TiO_2 electrodes in dye-sensitized solar cells for enhanced photocurrent. *J. Mater. Chem.* **22**, 17128-17132 (2012).
- 43 Wang, Y. *et al.* The photoelectrochemistry of transition metal-ion-doped TiO_2 nanocrystalline electrodes and higher solar cell conversion efficiency based on Zn^{2+} -doped TiO_2 electrode. *J. Mater. Sci.* **34**, 2773-2779 (1999).
- 44 Wang, G., Wang, Q., Lu, W. & Li, J. Photoelectrochemical study on charge transfer properties of TiO_2 -b nanowires with an application as humidity sensors. *J. Phys. Chem. B* **110**, 22029-22034 (2006).
- 45 Ling, Y. *et al.* Chemically modified titanium oxide nanostructures for dye-sensitized solar cells. *Nano Energy* **2**, 1373-1382 (2013).
- 46 Wang, G. *et al.* Hydrogen-treated TiO_2 nanowire arrays for photoelectrochemical water splitting. *Nano Lett.* **11**, 3026-3033 (2011).
- 47 Villarreal, T. L., Gómez, R., Neumann-Spallart, M., Alonso-Vante, N. & Salvador, P. Semiconductor photooxidation of pollutants dissolved in water: A kinetic model for distinguishing between direct and indirect interfacial hole transfer. I. Photoelectrochemical experiments with polycrystalline anatase electrodes under current doubling and absence of recombination. *J. Phys. Chem. B* **108**, 15172-15181 (2004).
- 48 Peterson, M. W., Turner, J. A. & Nozik, A. J. Mechanistic studies of the photocatalytic behavior of titania: Particles in a photoelectrochemical slurry cell and the relevance to photodetoxification reactions. *J. Phys. Chem.* **95**, 221-225 (1991).
- 49 Butler, M. A. & Ginley, D. S. Prediction of flatband potentials at semiconductor - electrolyte interfaces from atomic electronegativities. *J. Electrochem. Soc.* **125**, 228-232 (1978).
- 50 Boehm, H. P. & Herrmann, M. Über die chemie der oberfläche des titandioxids. I. Bestimmung des aktiven wasserstoffs, thermische entwässerung und rehydroxylierung. *Z. Anorg. Allg. Chem.* **352**, 156-167 (1967).
- 51 Turchi, C. S. & Ollis, D. F. Photocatalytic degradation of organic water contaminants: Mechanisms involving hydroxyl radical attack. *J. Catal.* **122**, 178-192 (1990).
- 52 Xu, W., Jain, P. K., Beberwyck, B. J. & Alivisatos, A. P. Probing redox photocatalysis of trapped electrons and holes on single sb-doped titania nanorod surfaces. *J. Am. Chem. Soc.* **134**, 3946-3949 (2012).
- 53 Zhang, Y. *et al.* Superresolution fluorescence mapping of single-nanoparticle catalysts reveals spatiotemporal variations in surface reactivity. *Proc. Natl. Acad. Sci. USA* **112**, 8959-8964 (2015).
- 54 Shen, H., Zhou, X., Zou, N. & Chen, P. Single-molecule kinetics reveals a hidden surface reaction intermediate in single-nanoparticle catalysis. *J. Phys. Chem. C* **118**, 26902-26911 (2014).
- 55 Kim, W., Tachikawa, T., Moon, G.-h., Majima, T. & Choi, W. Molecular-level understanding of the photocatalytic activity difference between anatase and rutile nanoparticles. *Angew. Chem. Int. Ed.* **53**, 14036-14041 (2014).
- 56 Lewis, N. S. Progress in understanding electron-transfer reactions at semiconductor/liquid interfaces. *J. Phys. Chem. B* **102**, 4843-4855 (1998).
- 57 Reichman, J. Collection efficiency of low - mobility solar cells. *Appl. Phys. Lett.* **38**, 251-253 (1981).
- 58 Chen, H., Wei, Z., Yan, K., Bai, Y. & Yang, S. Unveiling two electron-transport modes in oxygen-deficient TiO_2 nanowires and their influence on photoelectrochemical operation. *J. Phys. Chem. Lett.* **5**, 2890-2896 (2014).
- 59 Breckenridge, R. G. & Hosler, W. R. Electrical properties of titanium dioxide semiconductors. *Phys. Rev.* **91**, 793-802 (1953).
- 60 Tafalla, D., Salvador, P. & Benito, R. M. Kinetic approach to the photocurrent transients in water photoelectrolysis at n - TiO_2 electrodes: Ii . Analysis of the photocurrent - time dependence. *J. Electrochem. Soc.* **137**, 1810-1815 (1990).

- 61 Kumar, A. & Lewis, N. S. Short-wavelength spectral response properties of semiconductor/liquid junctions. *J. Phys. Chem.* **94**, 6002-6009 (1990).
- 62 Sze, S. M. (ed M. K. Lee) (Wiley, Hoboken, N.J. :, 2011).
- 63 Hirano, K. & Bard, A. J. Semiconductor electrodes: Xxviii . Rotating ring-disk electrode studies of photo - oxidation of acetate and iodide at. *J. Electrochem. Soc.* **127**, 1056-1059 (1980).
- 64 Zhong, D. K., Cornuz, M., Sivula, K., Gratzel, M. & Gamelin, D. R. Photo-assisted electrodeposition of cobalt-phosphate (co-pi) catalyst on hematite photoanodes for solar water oxidation. *Energy Environ. Sci.* **4**, 1759-1764 (2011).
- 65 El-Guibaly, F. & Colbow, K. Current-voltage characteristics of semiconductor-electrolyte junction solar-cells. *Can. J. Phys.* **59**, 1682-1685 (1981).
- 66 van de Lagemaat, J., Park, N. G. & Frank, A. J. Influence of electrical potential distribution, charge transport, and recombination on the photopotential and photocurrent conversion efficiency of dye-sensitized nanocrystalline tio₂ solar cells: A study by electrical impedance and optical modulation techniques. *J. Phys. Chem. B* **104**, 2044-2052 (2000).
- 67 Hill, D. J., Pinion, C. W., Christesen, J. D. & Cahoon, J. F. Waveguide scattering microscopy for dark-field imaging and spectroscopy of photonic nanostructures. *ACS Photonics* **1**, 725-731 (2014).
- 68 Powell, R. J. & Spicer, W. E. Optical properties of nio and coo. *Physical Review B* **2**, 2182-& (1970).
- 69 Abdi, F. F. & van de Krol, R. Nature and light dependence of bulk recombination in co-pi-catalyzed bivo₄ photoanodes. *J. Phys. Chem. C.* **116**, 9398-9404 (2012).
- 70 Jiang, C., Moniz, S. J. A., Khraisheh, M. & Tang, J. Earth-abundant oxygen evolution catalysts coupled onto zno nanowire arrays for efficient photoelectrochemical water cleavage. *Chem. Eu. J.* **20**, 12954-12961 (2014).